

Novel Insights into Sb-Cu Catalysts for Electrochemical Reduction of CO<sub>2</sub>

*Original*

Novel Insights into Sb-Cu Catalysts for Electrochemical Reduction of CO<sub>2</sub> / Zeng, J.; Fiorentin, M. R.; Fontana, M.; Castellino, M.; Risplendi, F.; Sacco, A.; Cicero, G.; Farkhondehfal, M. A.; Drago, F.; Pirri, C. F.. - In: APPLIED CATALYSIS. B, ENVIRONMENTAL. - ISSN 0926-3373. - ELETTRONICO. - 306:(2022), p. 121089. [10.1016/j.apcatb.2022.121089]

*Availability:*

This version is available at: 11583/2952774 since: 2022-01-25T08:33:02Z

*Publisher:*

Elsevier B.V.

*Published*

DOI:10.1016/j.apcatb.2022.121089

*Terms of use:*

This article is made available under terms and conditions as specified in the corresponding bibliographic description in the repository

*Publisher copyright*

Elsevier postprint/Author's Accepted Manuscript

© 2022. This manuscript version is made available under the CC-BY-NC-ND 4.0 license  
<http://creativecommons.org/licenses/by-nc-nd/4.0/>. The final authenticated version is available online at:  
<http://dx.doi.org/10.1016/j.apcatb.2022.121089>

(Article begins on next page)

# Novel Insights into Sb-Cu Catalysts for Electrochemical Reduction of CO<sub>2</sub>

Juqin Zeng<sup>a\*</sup>, Michele Re Fiorentin<sup>a</sup>, Marco Fontana<sup>a</sup>, Micaela Castellino<sup>b\*</sup>, Francesca Risplendi<sup>b</sup>, Adriano Sacco<sup>a</sup>, Giancarlo Cicero<sup>b\*</sup>, M.Amin Farkhondeh<sup>a</sup>, Filippo Drago<sup>c</sup>, Candido F. Pirri<sup>a,b</sup>

<sup>a</sup>Center for Sustainable Future Technologies @POLITO, Istituto Italiano di Tecnologia, Via Livorno 60, 10144 Turin, Italy

<sup>b</sup>Department of Applied Science and Technology, Politecnico di Torino, C.so Duca degli Abruzzi 24, 10129 Turin, Italy

<sup>c</sup>NanoChemistry, Istituto Italiano di Tecnologia, via Morego 30, 16163 Genoa, Italy

\*corresponding authors: [juqin.zeng@iit.it](mailto:juqin.zeng@iit.it), [micaela.castellino@polito.it](mailto:micaela.castellino@polito.it), [giancarlo.cicero@polito.it](mailto:giancarlo.cicero@polito.it)

**Keywords:** carbon dioxide; electrocatalysis; cuprous oxide; antimony; ab initio simulation

## Abstract

Catalysts play a vital role in electrochemical reduction of CO<sub>2</sub> to valuable products. Only based on effective catalysts, CO<sub>2</sub> electrolysis process can be advanced toward industrial application. In this work, we present a Sb-Cu<sub>2</sub>O material synthesized via one-pot microwave-assisted solvothermal route. The Sb-Cu<sub>2</sub>O derived bimetallic catalyst achieves a highest CO selectivity of 96% and good CO partial current densities of 37.3 and 74.0 mA cm<sup>-2</sup> at -0.8 and -1.2 V vs. reversible hydrogen electrode (RHE), respectively. The Sb-Cu catalyst also displays good stability at current densities ranging from 5.6 to 100 mA cm<sup>-2</sup>. Additionally, for the first time, a complete theoretical study reveals the critical roles of Sb in selective CO<sub>2</sub> conversion to CO on this bimetallic material, including stabilizing stepped Cu surfaces selective for the reaction, lowering energy barriers for the formation of key intermediate and favouring CO desorption.

## 1. Introduction

Excessive CO<sub>2</sub> emitted from burning fossil fuels is considered one of the main climate change causes. Strategies such as CO<sub>2</sub> capture and storage have been applied, aiming at decelerating and even at discontinuing the accumulation of CO<sub>2</sub> in the atmosphere. Further transformation of the captured CO<sub>2</sub> into fuels and chemicals is of crucial importance for a sustainable carbon cycle and the long-term energy storage. Among many technologies, electrochemical conversion is considered particularly attractive since it can use electricity generated from renewable sources as energy input [1-5]. This technology, although being very promising, confronts many challenges due to the high energy barriers, slow kinetics and complex pathways of the CO<sub>2</sub> reduction reaction (CO<sub>2</sub>RR). Therefore, rationally designed electrocatalysts are essential to boost the reaction and to tune the selectivity for a specific product. In the last decades, copper (Cu) has received the greatest attention as electrocatalytic material for the CO<sub>2</sub>RR, due to its unique properties from the early experimental studies by Hori *et al* [6, 7] as well as the computational investigations by Nørskov *et al* [8, 9] and Bagger *et al* [10]. Except bulk Cu and nanostructured Cu [11-15], Cu-based bimetallic systems have been widely explored and they demonstrated the most encouraging performance [16-19]. Among many secondary metals, post-transition metals such as tin (Sn), indium (In) and bismuth (Bi) are intensively studied since they alone are demonstrated to be active for the CO<sub>2</sub>RR and coupling them with Cu can catalyze the CO<sub>2</sub>RR to carbon monoxide (CO) and formate (HCOO<sup>-</sup>) selectively [20-25]. Even though antimony (Sb) is adjacent to these metals in the periodic table, it has attracted negligible attention in the community of the electrochemical CO<sub>2</sub>RR, probably due to the poor performance of the electrodeposited Sb reported earlier by Rosenthal *et al.* [26]. Until 2017, Zhang *et al.* [27] reported two-dimensional “few-layer” Sb nanosheets (SbNSs) that deliver a maximum faradaic efficiency (FE) of 84% and a maximum geometric current density of 3.1 mA cm<sup>-2</sup> for formate production at potentials from -0.7 V to -1.4 V vs. the reversible hydrogen electrode (RHE) in a CO<sub>2</sub>-saturated 0.5 M NaHCO<sub>3</sub> solution. In 2019, Sun *et al.* [28] synthesized Sb single atoms supported on N-doped porous carbon that reached an FE of about 82.0% and a highest current density of 2.4 mA cm<sup>-2</sup> for CO formation at -0.9 V vs. RHE in a CO<sub>2</sub>-saturated 0.1 M KHCO<sub>3</sub> solution. It is only very recently that Cu-Sb bimetallic materials were proposed for the CO<sub>2</sub>RR, achieving good CO selectivity of 85-90% [29-32] and moderate C<sub>2</sub>H<sub>4</sub> selectivity of 49.7% [33]. Among these work, only Cai *et al.* [32] performed a theoretical study through DFT calculations by designing a thermodynamic structure model of the Sb/Cu surface that considers the lattice mismatch between Cu and Sb at a high Sb coverage. The DFT study qualitatively consists with the in situ ATR-SEIRAS experimental observations, suggesting that the weak bonding of \*CO on Cu-Sb favors CO desorption and ultimately promotes CO formation. Despite the significance of this work, the good selectivity toward

CO production against the competing hydrogen evolution reaction (HER) and HCOOH formation, and the possible reaction pathways are not explained. So far, a thorough understanding of the electrochemical performance of Cu-Sb materials still calls for additional insights into the role of Sb and into the mechanisms of the competing CO<sub>2</sub>RR and HER.

The present study couples Sb and Cu for the CO<sub>2</sub>RR and, for the first time, explores the origin of the high CO selectivity and the reaction mechanism on the bimetallic catalyst through a complete theoretical study. Several Sb incorporated Cu<sub>2</sub>O powder-like materials were synthesized via a one-pot microwave-assisted solvothermal route. The optimal Sb-Cu catalyst derived from Sb-Cu<sub>2</sub>O is characterized by an outstanding CO selectivity (FE<sub>CO</sub> 90-95%) in a wide potential window from -0.7 V to -1.2 V vs. RHE in 0.1 M KHCO<sub>3</sub> aqueous electrolyte. With increasing KHCO<sub>3</sub> concentration, the good CO selectivity is maintained and a highest CO partial current density of 74.2 mA cm<sup>-2</sup> is observed. By means of *ab initio* simulations based on Density Functional Theory (DFT) and the Cluster Expansion (CE) method, we correlated the striking selectivity toward CO production to the change in Cu surface stability induced by Sb atoms. Under CO<sub>2</sub>RR conditions, Cu<sub>2</sub>O is reduced to metal Cu and Sb tends to segregate to the surface. Optimal surface concentrations of Sb appear to favor the exposure of stepped and reactive surface, on which CO<sub>2</sub> is selectively reduced to CO thanks to the lower kinetic barriers. In addition, the reaction mechanism was also illustrated by the theoretical study combining with electrokinetic experimental data.

## 2. Material and methods

### 2.1 Chemicals

Antimony(III) acetate (Sb(OAc)<sub>3</sub>, 99.99%), Copper(II) acetate hydrate (Cu(OAc)<sub>2</sub>·xH<sub>2</sub>O, 98.0%), potassium bicarbonate (KHCO<sub>3</sub>, 99.7%), ethylene glycol (EG, 99.8 %), Nafion<sup>®</sup> 117 solution (5 wt.%) and isopropanol were purchased from Sigma-Aldrich. Unless otherwise specified, all the materials were used as received in this work.

### 2.2 Synthesis of Sb-Cu<sub>2</sub>O materials

The pre-catalysts Sb-Cu<sub>2</sub>O were fabricated through a microwave-assisted solvothermal route. Four Sb-Cu<sub>2</sub>O materials were synthesized and named Sb<sub>x</sub>Cu<sub>2</sub>O (x = 0.11, 0.22, 0.33 and 0.55), where x was the nominal atomic ratio of Sb(OAc)<sub>3</sub>/Cu(OAc)<sub>2</sub> in the precursor solution. Two samples with only Sb or Cu precursor were also prepared and named Sb<sub>2</sub>O<sub>3</sub> and Cu<sub>2</sub>O, respectively. The details of the synthesis are shown in the *Synthesis* section and Table S1 of the supporting information.

### 2.3 Physical and chemical characterizations

The morphology was studied by Field Emission Scanning Electron Microscopy (FESEM, ZEISS Supra 40). X-ray diffraction (XRD) was performed in Bragg-Brentano symmetric geometry by using a PANalytical X'Pert Pro instrument (Cu-K $\alpha$  radiation, 40 kV and 30 mA) equipped with an X'Celerator detector. MAUD software [34] was used for full XRD pattern fitting based on the Rietveld method (*XRD characterization* section of supporting information). Transmission Electron Microscopy (TEM) was carried out on a FEI Tecnai G2 F20 S-Twin instrument, operated at 200 kV acceleration voltage. The microscope is equipped with a EDAX detector (30 mm<sup>2</sup> active area, Si(Li) technology) for Energy-Dispersive X-ray spectroscopy (EDX). Regarding TEM sample preparation, the dry powders were dispersed in high-purity ethanol, sonicated for 30 min and subsequently drop-casted on Au holey carbon grids. The sonication time was chosen in accordance with the electrode preparation procedure. X-ray photoelectron spectroscopy (XPS) analysis has been performed by means of a PHI 5000 Versaprobe spectrometer, equipped with a monochromated Al K-alpha source (1486.6 eV). A double charge compensation system, comprised of an electron and Ar<sup>+</sup> ion gun, was used to neutralize surface charging. Survey and high resolution (HR) spectra were acquired using Pass Energy (PE) values of 187.85 and 23.50 eV, respectively. C1s peak at 284.5 eV was chosen as the reference shift. Tougaard background function was subtracted from HR spectra to remove background signal and pseudo-Voigt functions were used to deconvolute the HR curves. Casa XPS Version 2.3.18 dedicated software has been used to analyze the raw spectra.

## 2.4 Electrode preparation, electrochemical tests and product analyses

The pre-catalysts were coated onto a carbon paper, as detailed in the *Electrode preparation* section of supporting information, in order to enable the electrochemical evaluation of the materials toward the CO<sub>2</sub>RR. Cyclic voltammetry (CV), linear sweep voltammetry (LSV) and electrochemical impedance spectroscopy (EIS) were performed in a three-electrode single-compartment cell at room temperature with a CHI760D electrochemical workstation, as described in the *Electrochemical characterizations* section of supporting information.

The CO<sub>2</sub>RR experiments in KHCO<sub>3</sub> electrolyte were conducted in a custom-made H-type cell (Figure S1a) and those in KOH electrolyte were carried out in a custom-made flow cell (Figure S1b), Chronoamperometric (CA) technique was applied for the CO<sub>2</sub>RR with a CHI760D electrochemical workstation. The *Electrochemical characterizations* section of supporting information shows the details of the cells and processes. The reported potentials were corrected by compensating 85% of the ohmic drop (iR-compensation). Electrode potentials after iR-compensation were rescaled to the RHE reference by applying Nernst equation,  $E_{vs.RHE} = E_{vs.Ag/AgCl} + E_{Ag/AgCl(3M\ Cl^-)} + 0.0591 \times pH$ .

Gas-phase products were analyzed on-line with a micro gas chromatograph ( $\mu$ GC, Fusion®, INFICON) and liquid products were analyzed by a High Performance Liquid Chromatograph

(ThermoFischer Ultimate 3000), as detailed in the *Product analysis* section of supporting information.

## **2.5 Mass transport model**

The local concentrations of  $\text{CO}_2$  and  $\text{HCO}_3^-$  in proximity of the electrode ( $[\text{CO}_2]_{\text{local}}$  and  $[\text{HCO}_3^-]_{\text{local}}$ ) in different bulk  $[\text{HCO}_3^-]$  electrolytes were calculated employing the mass transport model described in details in our previous work [35]. The diffusion coefficients and the equilibrium concentrations of various chemical species as well as the electrolyte viscosity are dependent on the bulk  $[\text{HCO}_3^-]$  and different values were used for 0.1 M, 0.5 M, 1.0 M and 2.0 M  $\text{KHCO}_3$  electrolyte [36]. Correction was not made for the effect of ionic strength on  $\text{CO}_2$  solubility.

## **2.6 Computational methods**

When working under potentials and pH values suitable for  $\text{CO}_2$  electroreduction, Cu oxides are rapidly reduced to metallic Cu [37], whose most stable surface can then be assumed to be most largely involved in the  $\text{CO}_2\text{RR}$ . However, the presence of Sb atoms dispersed in metallic Cu can significantly affect the surface stability and, in turn, the activity and selectivity of the catalyst. The prediction of the structure and stability of Sb modified Cu surfaces has been carried out by combining DFT and CE methods. CE simulations were performed by employing the ATAT software [38], while for the DFT calculations the QUANTUM ESPRESSO software package was used [39, 40]. The coupled CE-DFT approach makes it possible to accurately predict concentration-dependent phase diagrams and surface phase diagrams of a given alloy, following a step-by-step process based on alternating DFT total energy calculations and CE structural predictions [41]. Details on this procedure can be found in the Supporting Information and in the literature [42, 43]. The analysis of electrochemical reactions on the catalyst was carried out within the computational hydrogen electrode framework [44], which allows obtaining reaction free energies as a function of the applied potential. A correction to the adsorbate free energies was added to account for solvation effects due to the aqueous environment [8]. Activation barriers for each reduction reaction step were obtained with nudged elastic band (NEB) calculations at the equilibrium potential of the relative step, and their values at different potentials were derived within the Butler-Volmer formalism [45-47]. Activation barriers for the HER were obtained from the literature [48].

# **3. Results and Discussion**

## **3.1 Synthesis and characterization of $\text{SbxCu}_2\text{O}$ pre-catalysts**

Figure 1a illustrates the synthesis of pre-catalysts via one-pot microwave-assisted solvothermal method. The obtained  $\text{Cu}_2\text{O}$  sample is composed of submicrometric cubic and micrometric polyhedral aggregates with irregular external surface populated by nanoplatelets (Figure 1b and inset of Figure 1b). The addition of Sb has remarkable effect on the morphology of the materials. Uniform and large spheres (diameter in the range of 4-7  $\mu\text{m}$ ) are formed in all Sb- $\text{Cu}_2\text{O}$  materials (Figure 1c-f) and these spheres consist of loosely packed nanoparticles with diameter less than 15 nm (inset of Figure 1c-f). The spheres become less compact with increasing the percentage of Sb salt in the precursor solution. The  $\text{Sb}_2\text{O}_3$  sample contains submicrometric rhombohedral particles with a wide size distribution from 500 nm to 800 nm (Figure 1g). It is worth noting that similar particles of Sb species are also present in the  $\text{Sb}_{0.55}\text{Cu}_2\text{O}$  sample, while these particles are absent in the other Sb- $\text{Cu}_2\text{O}$  materials.

XRD analysis has been employed to identify the crystalline phase compositions of the materials. The patterns of various materials and the fitting results obtained by Rietveld refinement are shown in Figure S2 and Table S2. For the  $\text{Cu}_2\text{O}$  sample, all peaks are associated to the (110), (111), (200), (211), (220), (311) and (222) planes of  $\text{Cu}_2\text{O}$  with a cubic structure (JCPDS 00-005-0667). The  $\text{Cu}_2\text{O}$  phase has a bimodal crystallite size distribution centered at  $307 \pm 33$  nm and  $35 \pm 5$  nm. The  $\text{Sb}_2\text{O}_3$  sample exhibits peaks related to only the cubic  $\text{Sb}_2\text{O}_3$  (JCPDS 01-071-0365) structure, with a refined crystallite size of  $191 \pm 1$  nm. All Sb- $\text{Cu}_2\text{O}$  materials show peaks corresponding to the cubic  $\text{Cu}_2\text{O}$  phase. No peaks related to crystalline Sb species are observed for the  $\text{Sb}_{0.11}\text{Cu}_2\text{O}$ ,  $\text{Sb}_{0.22}\text{Cu}_2\text{O}$  and  $\text{Sb}_{0.33}\text{Cu}_2\text{O}$  samples, while peaks associated to  $\text{Sb}_2\text{O}_3$  crystallite phase are present in the XRD pattern of the  $\text{Sb}_{0.55}\text{Cu}_2\text{O}$  sample. The  $\text{Cu}_2\text{O}$  crystallites in the  $\text{Sb}_{0.11}\text{Cu}_2\text{O}$  sample display a bimodal size distribution centered at  $86 \pm 4$  nm and  $9 \pm 1$  nm and the crystallite size values for the  $\text{Sb}_{0.22}\text{Cu}_2\text{O}$ ,  $\text{Sb}_{0.33}\text{Cu}_2\text{O}$  and  $\text{Sb}_{0.55}\text{Cu}_2\text{O}$  samples are estimated as  $15 \pm 2$  nm,  $12 \pm 4$  nm and  $14 \pm 1$  nm, respectively. In addition to  $\text{Cu}_2\text{O}$ , the  $\text{Sb}_{0.55}\text{Cu}_2\text{O}$  sample also contains cubic  $\text{Sb}_2\text{O}_3$  crystalline phase with an estimated crystallite size of  $109 \pm 5$  nm, which is slightly smaller than those in the  $\text{Sb}_2\text{O}_3$  sample. The detailed XRD analysis unveils that the addition of Sb has dramatically reduced the crystallite size of the  $\text{Cu}_2\text{O}$  phase and that its incorporation up to a high nominal content of 25 at.% ( $\text{Sb}_{0.33}\text{Cu}_2\text{O}$  sample) has not resulted in crystalline Sb species. It is further noticed that the lattice constant is slightly altered due to the Sb incorporation, with a percentage variation lower than 0.5 % for the Sb- $\text{Cu}_2\text{O}$  samples with respect to the  $\text{Cu}_2\text{O}$  sample (Table S2). Even though the insignificant variation in the lattice parameter, it is not ruled out that Sb could be successful incorporated into  $\text{Cu}_2\text{O}$  crystal host at high concentrations, due to the similar radius size of Sb(III) with that of Cu(I) [49-51].

The uniform incorporation of Sb in the  $\text{Cu}_2\text{O}$  crystalline phase has further been investigated for the  $\text{Sb}_{0.22}\text{Cu}_2\text{O}$  sample by means of TEM, through Selected Area Electron Diffraction (SAED), high-resolution (HR) TEM imaging and EDX elemental maps. Since the micrometric spheres of  $\text{Sb}_{0.22}\text{Cu}_2\text{O}$  are not electron transparent, the powder sample was sonicated for 30 min before TEM

analysis in order to detach some nanometric particles which constitute the micro-spheres. Representative results for the TEM characterization are provided in Figure 2. The sonication procedure allows to obtain electron-transparent regions (Figure 2a) from which it is possible to acquire SAED patterns, such as the one shown in Figure 2b. The presence of diffraction rings is characteristic of the polycrystalline nature of the material and careful analysis of the diffraction pattern (Table S3) confirms that the crystalline phase is  $\text{Cu}_2\text{O}$ , without any signature of  $\text{Sb}_2\text{O}_3$  phase, in accordance with XRD results. Nanoscale structural analysis by HRTEM (Figure 2c-e) shows that  $\text{Cu}_2\text{O}$  crystallites have a characteristic size in accordance with the one ( $15 \pm 2$  nm) obtained from the Rietveld analysis of XRD data. Moreover, analysis of HRTEM images confirms the absence of  $\text{Sb}_2\text{O}_3$  phase and suggests the incorporation of Sb in the  $\text{Cu}_2\text{O}$  crystalline phase. Further indication is obtained by EDX elemental mapping. Figure 2f presents a High-Angle Annular Dark-Field (HAADF) Scanning Transmission Electron Microscopy (STEM) image, coupled with its corresponding elemental Cu and Sb maps. Since the elemental contrast in both EDX maps correlates with the atomic-number contrast (Z-contrast) of the HAADF image, it is reasonable to assume that Sb is uniformly incorporated into the  $\text{Cu}_2\text{O}$  nanostructures at the nanoscale. It is important to notice that elemental distribution (EDX maps) and structural information (HRTEM analysis at the edges) were also obtained for the microspheres (Figure S3) and these results are in accordance with the ones obtained from the electron-transparent regions. Hence, it is possible to state the Sb distribution is homogeneous at both nanometric and micrometric scales.

XPS measurements have been performed on the  $\text{Sb}_2\text{O}_3$ , Sb- $\text{Cu}_2\text{O}$  and  $\text{Cu}_2\text{O}$  samples to investigate the chemical composition of the surface. From the survey spectra, Cu, Sb, O and C are the main elements for all Sb- $\text{Cu}_2\text{O}$  samples (Table S4). It is important to note that the Sb/Cu atomic ratios are close to the nominal ones, especially for the Sb0.11 $\text{Cu}_2\text{O}$ , Sb0.22 $\text{Cu}_2\text{O}$  and Sb0.33 $\text{Cu}_2\text{O}$  samples. Detailed information on the oxidation states of Sb and Cu elements on the Sb0.22 $\text{Cu}_2\text{O}$  sample have been obtained from HR analysis (Figure 3). In order to get information from the Sb3d doublet, we had to deconvolute its signal starting from Sb3d<sub>3/2</sub> peak, since the Sb3d<sub>5/2</sub> overlaps with O1s signal. Hence, the intensity and binding energy of Sb3d<sub>5/2</sub> peak have been set by the Sb3d<sub>3/2</sub> peak's position and intensity, according to the spin-orbit splitting ( $\Delta = 9.39$  eV) and ratio (0.7), and the remaining area in the Sb3d<sub>5/2</sub> peak is attributed to O 1s signal. As shown in Figure 3a, the Sb3d doublet shows only one oxidation state related to Sb(III) [52]. O1s contribution has been deconvoluted in three peaks associated to metal oxide (530 eV), C=O (~531 eV) and C-O (~532 eV), in which the latter two are due to ambient contamination (adsorbates). The Cu2p doublet represents always a tricky region to be analyzed, since Cu(I) and Cu(0) are commonly reported at the same binding energy, while Cu(II) is well recognizable due to the presence of its satellite between 940 and 945 eV. To overcome this issue, Auger CuLMM region has also been acquired to enable the calculation of the Auger parameter, which



can help to understand the average Cu oxidation state. From the Cu2p<sub>3/2</sub> position (932.5 eV) and small satellite at 942 eV (Figure 3b), we can appreciate the presence of main Cu(I) oxidation state with minor Cu(II) [53]. From the maximum position ( $E_K = 916.8$  eV) of the CuLMM peak (inset of Figure 3b), an Auger parameter of 1848.8 eV is obtained (Table S5) and it is commonly attributed to Cu(I) [53], in accordance with the XRD and TEM analyses. Cu(II) is absent in the diffraction analyses, probably due to their low amount or their amorphous phase [54, 55]. The oxides in the upmost layer can be formed due to the exposure to atmosphere [54, 56]. Other Sb-Cu<sub>2</sub>O samples possess similar surface chemical characteristics with respect to the Sb<sub>0.22</sub>Cu<sub>2</sub>O, except that all these samples have notable differences in the surface atomic ratio of Sb/Cu, as shown in Table S4 and S5. With raising the ratio of the Sb/Cu salts in the precursor solution, the Sb percentage on the Sb-Cu<sub>2</sub>O surface increases and the Sb content quantified by the inductively coupled plasma optical emission spectroscopy (ICP-OES) analysis rises as well (Table S6). The monometallic samples, Cu<sub>2</sub>O and Sb<sub>2</sub>O<sub>3</sub>, are also analyzed (Figure S4 and S5). The surface of Cu<sub>2</sub>O sample is rich of Cu (II) and thus is more oxidized compared to that of Sb-Cu<sub>2</sub>O samples, while the Sb element on the Sb<sub>2</sub>O<sub>3</sub> sample shows Sb(III) as the only oxidation state as observed on the Sb-Cu<sub>2</sub>O samples.

### 3.2 Comparison of CO<sub>2</sub>RR activity on Sb-Cu<sub>2</sub>O derived catalysts

Voltammetric study has been performed at various electrodes in a CO<sub>2</sub>-saturated 0.1 M KHCO<sub>3</sub> electrolyte in order to study the electrochemical characteristics of the materials. Unless otherwise specified, all potentials refer to the RHE in this work. From cyclic voltammograms in Figure S6a and S6b, the electrodes with Cu<sub>2</sub>O and Sb<sub>2</sub>O<sub>3</sub> show characteristic redox peaks of Cu and Sb species, respectively. All electrodes with Sb-Cu<sub>2</sub>O show a cathodic peak attributed to the reduction of Sb species, and this peak increases in intensity from the electrode with Sb<sub>0.11</sub>Cu<sub>2</sub>O to that with Sb<sub>0.55</sub>Cu<sub>2</sub>O (Figure S6c). On contrast, the redox peak of Cu species at high potential range shows an opposite trend. This outcome is in accordance with the surface composition of the materials, that is, Sb increases and Cu decreases from Sb<sub>0.11</sub>Cu<sub>2</sub>O to Sb<sub>0.55</sub>Cu<sub>2</sub>O. The reduction peaks of Sb and Cu cations indicate that both Cu and Sb oxides are (partially) reduced at potentials more positive than those where the CO<sub>2</sub>RR experiments were conducted in this work ( $\leq -0.4$  V). Hence, under the CO<sub>2</sub>RR conditions, the Sb<sub>2</sub>O<sub>3</sub>, Cu<sub>2</sub>O and Sb-Cu<sub>2</sub>O (Sb<sub>x</sub>Cu<sub>2</sub>O) materials are restructured to form real catalysts, and the electrodes prepared with these materials are named Sb, Cu and Sb-Cu (Sb<sub>x</sub>Cu), respectively.

Figure S6d shows the linear sweep voltammograms of various electrodes in the potential range where the CO<sub>2</sub>RR and its competing HER occur. All Sb-Cu electrodes display much lower onset potentials compared to the Cu one and they show much smaller current density with respect to the Sb electrode at low potentials ( $< -0.85$  V), demonstrating notable differences among the bimetallic and

monometallic electrodes. Since the current normalized by geometric surface area of the electrode does not reflect the activity of the catalyst, we calculated the current normalized by the electrochemically active surface area (ECSA), as detailed in Table S7 and Figure S7. As shown in Figure S6e, the activity of these catalysts toward the reduction reactions follows a trend,  $\text{Cu} \gg \text{Sb0.11Cu} > \text{Sb0.22Cu} > \text{Sb0.33Cu} \approx \text{Sb0.55Cu}$ , at potentials lower than -0.55 V. It is clear that addition of Sb decreases the overall activity of Cu catalyst toward the reduction reactions and an increase in the Sb content leads to a decrease in the activity of the Sb-Cu catalyst. The Sb catalyst shows slow activity at potentials higher than -0.75 V and displays a fast increase in activity with lowering the potential in the more negative potential range. With respect to the Sb, the Sb-Cu catalysts show similar onset potentials but much lower activity in the low potential range ( $< -0.9$  V). This outcome implies that the Sb-Cu catalysts are also distinct from the Sb one toward the reduction reactions.

In order to understand the differences in the activity and selectivity among the Cu, Sb-Cu and Sb catalysts for the  $\text{CO}_2\text{RR}$ , CA measurements were carried out in a three-electrode H-type cell (Figure S1a) in a  $\text{CO}_2$ -saturated 0.1 M  $\text{KHCO}_3$  solution. Typical i-t curves and product analyses are shown in Figure S8. Various electrodes are compared in Figure 4a and 4b at -0.8 V and -1.0 V, respectively, in terms of both selectivity and geometric activity. The Cu electrode has poor selectivity for the  $\text{CO}_2\text{RR}$ , with  $\text{FE}_{\text{CO}}$  below 10% and  $\text{FE}_{\text{HCOOH}}$  below 6% at both potentials. In contrast, at the Sb electrode, the  $\text{HCOOH}$  selectivity reaches a considerable value of 40% at -0.8 V and it becomes less significant at -1.0 V, while no trace of CO is detected at both potentials. Differing from the Cu and Sb electrodes, the Sb-Cu ones mainly produce CO with minor  $\text{HCOOH}$ . Particularly, the Sb0.22Cu and Sb0.33Cu demonstrate a good selectivity for CO and relatively high geometric current densities at both potentials. The ECSA-normalized current densities on each electrode at -0.8 V and -1.0 V are shown in Figure 4c and 4d, respectively. The Cu catalyst has much higher activity for the  $\text{H}_2$  formation compared to that for CO and  $\text{HCOOH}$  formation, as evidenced by a normalized partial current density for  $\text{H}_2$  10-20 times larger than those for the latter two. With addition of 9.6 at.% of Sb (Sb0.11Cu sample), the formation of both  $\text{H}_2$  and  $\text{HCOOH}$  is dramatically suppressed, while the CO formation is impressively boosted. With respect to the Cu catalyst, the Sb0.11Cu reduces the activity for  $\text{H}_2$  formation by 15 times at -0.8 V and by 6 times at -1.0 V, while it increases the activity for CO formation by 4-5 times. A further increase of Sb content leads to declined activity for CO formation but sustained inhibition of both  $\text{HCOOH}$  and  $\text{H}_2$  formation at the Sb0.22Cu and Sb0.33Cu catalysts. Concerning the total activity for both  $\text{CO}_2\text{RR}$  and HER, with respect to the Cu catalyst, 9.6 at.% of Sb addition leads to a significant decrease of 50-60% and further Sb addition results in a tremendous decrease of 75%, as also observed from the linear sweep voltammetry analysis. The Sb0.11Cu catalyst shows the highest activity for CO formation (Figure 4c and 4d), while its electrode shows much lower

geometric activity than the Sb0.22Cu and Sb0.33Cu electrodes (Figure 4a and 4b), due to the much smaller ESCA of the former (Table S7). From comparison, the Sb0.22Cu electrode demonstrates the best selectivity and highest geometric current densities for CO formation.

### 3.3 CO<sub>2</sub> electrolysis on the Sb0.22Cu sample

Further investigations have been performed at the Sb0.22Cu electrode in a wide potential range from -0.5 V to -1.2 V in 0.1 M KHCO<sub>3</sub> electrolyte. As shown in Figure 5a, the Sb0.22Cu electrode exhibits good potential for converting CO<sub>2</sub> to CO. It is the main product from the CO<sub>2</sub>RR and becomes dominant at potentials lower than -0.5 V. The CO selectivity is characterized by an FE value of about 85% at -0.6 V (overpotential  $\eta$  = 490 mV) and enhanced up to 90-95% from -0.7 V to -1.2 V ( $\eta$  = 690 - 990 mV). The FE<sub>H<sub>2</sub></sub> maintains at low values ( $\leq$  7%) from -0.7 V to -1.2 V and the FE<sub>HCOOH</sub> formation occupies even lower FE (1-3%) at potentials more negative than -0.7 V. The current density for CO formation is 0.41 mA cm<sup>-2</sup> at -0.5 V and it rapidly increases to 15.2 mA cm<sup>-2</sup> at -1.2 V. The obtained current densities are in the range of reported values in aqueous CO<sub>2</sub> system with similar electrolytes and the low values are attributed to the limited reducible CO<sub>2</sub> in aqueous electrolyte [57, 58]. The long-term stability of the Sb0.22Cu electrode was further evaluated at -0.8 V, as shown in Figure 5b. During a 45-hour test, the production rate of CO shows a good retention of about 93%, decreasing from about 0.086 mmol cm<sup>-2</sup> h<sup>-1</sup> at the first hours to approximately 0.08 mmol cm<sup>-2</sup> h<sup>-1</sup> at the end. The FE<sub>CO</sub> displays a similar trend and it decreased from 94% to 90% during the test. The good retention of the electrode indicates satisfactory durability of Sb0.22Cu under working conditions.

The performance of the Sb0.22Cu electrode for the CO<sub>2</sub>RR to CO has been studied in KHCO<sub>3</sub> electrolyte with various concentrations. As shown in Figure 6a-c, the selectivity of the electrode is slightly affected by the KHCO<sub>3</sub> concentration from -0.6 V to -0.9 V and excellent FE values (90-96%) for CO formation are obtained in all electrolytes. At potentials higher than -0.6 V, the CO selectivity is slightly enhanced as increasing the KHCO<sub>3</sub> concentration until 1.0 M, while the CO formation is less favored at potentials lower than -0.9 V when increasing the KHCO<sub>3</sub> concentration to 2.0 M. In contrast to the selectivity, the electrode activity is dramatically influenced by the electrolyte composition and it is significantly boosted by increasing the KHCO<sub>3</sub> concentration at each potential. In 2.0 M KHCO<sub>3</sub> electrolyte, the Sb0.22Cu electrode achieves CO partial current density densities of 37.3 mA cm<sup>-2</sup> and 74.0 mA cm<sup>-2</sup> at -0.8 V and -1.2 V, respectively. The Sb0.22Cu electrode was also tested in KOH electrolyte with a flow reactor (Figure S1b) and it can produce a CO partial current density of approximately 60 mA cm<sup>-2</sup> at -0.8 V (Figure S9), which is even superior to the highest value obtained in KHCO<sub>3</sub> electrolyte at the same potential, implying that this electrode could be suitable to be applied in a wide range of electrolytes. Figure 6d-f show the selectivity of the

main gas products and CO partial current density on the Sb0.22Cu electrode at -0.8 V in KHCO<sub>3</sub> electrolyte during prolonged tests. It is demonstrated that the electrode possesses good stability in terms of selectivity and activity in KHCO<sub>3</sub> electrolyte with various concentrations. Together with the prolonged tests at -1.2 V (Figure S10), it is possible to state that the Sb0.22Cu electrode possesses good durability at various current densities ranging from 5.6 mA cm<sup>-2</sup> to 100 mA cm<sup>-2</sup>. By comparison with other reported CO-selective catalysts (Table S8), it is evident that the herein proposed Sb-Cu material shows outstanding performance for the CO<sub>2</sub>RR to CO in terms of selectivity, activity and durability.

Finally, to study the effect of [HCO<sub>3</sub><sup>-</sup>], we performed the CO<sub>2</sub> electrolysis at a constant potential of -0.8 V in electrolytes with various [HCO<sub>3</sub><sup>-</sup>] ranging from 0.05 to 2.0 M. As shown in Figure 7a, the CO<sub>2</sub>RR to CO rate increases with increasing the HCO<sub>3</sub><sup>-</sup> concentration. A plot of log ( $j_{\text{CO}}$ ) in function of log ([HCO<sub>3</sub><sup>-</sup>]<sub>bulk</sub>) shows a slope of 0.8, indicating approximately first-order dependence of the reaction rate on the [HCO<sub>3</sub><sup>-</sup>]<sub>bulk</sub>. Based on this outcome, it is widely accepted that the HCO<sub>3</sub><sup>-</sup> ions act as proton donors and participate in the CO<sub>2</sub>RR to CO [59-62]. However, Dunwell *et al.* [63] found that replacing the HCO<sub>3</sub><sup>-</sup> with other similar proton donors such as [HPO<sub>4</sub><sup>2-</sup>] fails to maintain the first-order dependence of the reaction rate on the [HPO<sub>4</sub><sup>2-</sup>], suggesting that the primary role of the HCO<sub>3</sub><sup>-</sup> ions could be not proton donor. They proposed that HCO<sub>3</sub><sup>-</sup> enhances the CO<sub>2</sub>RR to CO rate by increasing the availability of CO<sub>2</sub> near the electrode surface ([CO<sub>2</sub>]<sub>local</sub>) through rapid equilibrium between HCO<sub>3</sub><sup>-</sup> and dissolved CO<sub>2</sub>. To correlate [CO<sub>2</sub>]<sub>local</sub> and [HCO<sub>3</sub><sup>-</sup>]<sub>local</sub> with [HCO<sub>3</sub><sup>-</sup>]<sub>bulk</sub>, we employed a diffusion model reported in our previous work [35], taking into consideration the bubble-induced mass transport near the electrode. The model is based on fitting the experimental data reported in Figure 5a and 6a-c. The evaluation of the size of gas bubbles is the basic step of the bubble-induced mass transport modelling. The bubble aperture diameters able to give the best fits between the experimental data and the calculated CO partial current density-potential curves are found to be equal to 500 μm, 75 μm, 20 μm and 10 μm in 0.1 M, 0.5 M, 1.0 M and 2.0 M KHCO<sub>3</sub> electrolyte, respectively, as shown in Figure S11. The bubble-induced mass transport model then proceeded with the values of the bubble aperture diameters, as detailed in our previous work [35]. As shown in Figure S12, the [CO<sub>2</sub>]<sub>local</sub> quickly decreases with lowering the applied potentials in each electrolyte and it increases as raising the [HCO<sub>3</sub><sup>-</sup>]<sub>bulk</sub> at the same potential in the high overpotential range (-1.0 V - -1.2 V). In contrast, the [HCO<sub>3</sub><sup>-</sup>]<sub>local</sub> shows a slower decrease while negatively shifting the potential and it remains significantly higher in larger [HCO<sub>3</sub><sup>-</sup>]<sub>bulk</sub> solution (Figure S13). The [CO<sub>2</sub>]<sub>local</sub> and [HCO<sub>3</sub><sup>-</sup>]<sub>local</sub> are plotted as function of [HCO<sub>3</sub><sup>-</sup>]<sub>bulk</sub> at -1.2 V where the reaction rate is the highest in each [HCO<sub>3</sub><sup>-</sup>]<sub>bulk</sub> electrolyte (Figure 7b). It is clear that a higher [HCO<sub>3</sub><sup>-</sup>]<sub>bulk</sub> dramatically enhances both [CO<sub>2</sub>]<sub>local</sub> and [HCO<sub>3</sub><sup>-</sup>]<sub>local</sub>. When plotting log [CO<sub>2</sub>]<sub>local</sub> in function of log [HCO<sub>3</sub><sup>-</sup>]<sub>local</sub>, a slope of 1.0 is obtained, as shown in Figure 7c. The first-order dependence of

$[\text{CO}_2]_{\text{local}}$  on  $[\text{HCO}_3^-]_{\text{local}}$  reflects significant relevance between reducible  $\text{CO}_2$  and  $\text{HCO}_3^-$  ions, indicating that the enhancement of the  $\text{CO}_2\text{RR}$  to  $\text{CO}$  rate by increasing  $[\text{HCO}_3^-]_{\text{bulk}}$  is likely attributed to the improvement of  $\text{CO}_2$  availability near the electrode surface.

### ***3.4 Characterizations of the tested electrodes***

Further analyses have been performed on the tested Sb, Cu and Sb0.22Cu electrodes in order to investigate the restructuring of the materials. XRD analysis shows that metallic Cu and  $\text{Cu}_2\text{O}$  are observed in the reduced Cu and Sb0.22Cu electrodes (Figure S14). No evidence of crystalline Sb species is observed in the Sb0.22Cu electrode, while only diffraction peaks associated to metallic Sb appear in the Sb electrode. XPS analysis evidences that only Cu(0) and Sb(III) exist on the surface of the Sb0.22Cu electrode (Figure S15a-c), and Sb(III) is partially reduced to Sb(0) on the surface of the Sb electrode (Figure S15d). Based on these results, it is believed that the small quantity of  $\text{Cu}_2\text{O}$  detected by XRD can be formed during the sample preparation and the ex-situ measurement in air, and Cu oxides are fully reduced to metallic Cu under negative potentials for the  $\text{CO}_2\text{RR}$ , which is consistent with the widely reported results obtained by in-situ/operando techniques [64-68]. Regarding the Sb species under the  $\text{CO}_2\text{RR}$  conditions, it is convincing that Sb(0) is formed, while it is impossible to exclude the coexistence of cationic Sb with the herein used ex-situ techniques.

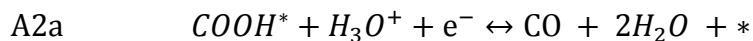
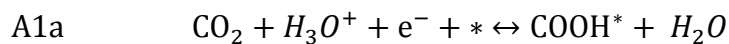
### ***3.5 Mechanism study of the $\text{CO}_2\text{RR}$ to $\text{CO}$ on Sb-Cu materials***

To elucidate the mechanism of  $\text{CO}_2\text{RR}$  on Sb-Cu samples, it is important to primarily determine the geometry of the most stable catalyst surface, on which the electrochemical reactions are likely to take place. Thermodynamic data and above-mentioned discussion suggest that Cu(I) in the as-synthesized catalyst is reduced to Cu(0) under catalytic conditions. Among the possible Cu surfaces, we focused on terraced Cu(111), the most stable surface exposed by pristine metallic Cu, and on Cu(211), as representative of higher energy stepped structure. By means of DFT calculations, we found that for both (111) and (211) terminations, Sb atoms prefer to segregate toward the outer surface layers since the configuration containing the dopant atom in the top surface layer is thermodynamically more stable compared to sub-surface positions (energy gain of 2.10 eV). Furthermore, the formation of Sb clusters on the surface is found to be thermodynamically unfavored, confirming the finding based on TEM and EDX maps analysis (Figure 2). A combined DFT and CE approach was employed to predict the structural properties of  $\text{Sb}_x\text{Cu}_{(1-x)}$  alloys and to compare the

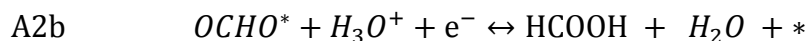
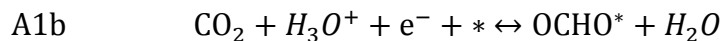
stability of  $\text{Sb}_x\text{Cu}_{(1-x)}(111)$  and  $\text{Sb}_x\text{Cu}_{(1-x)}(211)$  surfaces. A null surface concentration ( $x=0$ ) consists of pure Cu surfaces while a surface concentration  $x=1$  corresponds to a Cu surface where all exposed Cu atoms are substituted by Sb atoms. Results of CE performed on both surfaces are plotted in Figure S16, showing the DFT calculated surface formation energy  $\gamma_{\text{form}}$  used for the CE fitting together with the resulting predicted  $\gamma_{\text{form}}$  from the CE. The Cu(211) surface CE is plotted in blue, Cu(111) surface CE in red, and the dashed lines represent all the ground states throughout the phase diagram. From Figure S16 it is possible to notice that as Sb is added to the Cu surface layer, the formation energy of the  $\text{Sb}_x\text{Cu}_{(1-x)}(111)$  surface increases monotonically, while formation energy of the  $\text{Cu}_{(1-x)}\text{Sb}_x(211)$  surface decreases, reaching a minimum at  $x=0.5$ . The effect of Sb atoms is therefore the stabilization of the stepped (211) surface with respect to the flat (111). Moving from  $x=0$  to  $x=1$ , the most stable  $\text{Sb}_x\text{Cu}_{(1-x)}(211)$  surface structures consist of a progressive Sb substitution of Cu atoms starting from the edge of the steps in such a manner that each Sb first-neighbor site is occupied by a Cu atom, as shown in Figures 9b-c, confirming the Sb tendency to prefer undercoordinated positions. Sb atoms introduce distortions in the surface plane that alter the initial atomic arrangement and allow for outward relaxation of Sb atoms. In  $\text{Sb}_x\text{Cu}_{(1-x)}(211)$  structures with  $x \geq 0.5$  the surface reconstruction is such to expose Sb atoms only. As confirmed by the experiments, DFT calculations predict that Sb activity in the  $\text{CO}_2\text{RR}$  is extremely low (see Supporting Information, Table S9), therefore high Sb concentrations ( $x \geq 0.5$ ) prevent the interactions between reactants and Cu active sites, thus hindering the electrocatalytic performances. For these reasons, we argue that the most likely surface concentration values of the active catalysts will fall around intermediate values ( $0.2 < x < 0.5$ ) at which the (211) surface is stabilized and not yet covered by a full Sb monolayer. In the study of the reaction mechanism, we considered the (211) surface at  $x=0.33$ .

To enable the mechanism study, we then obtained the electrokinetic experimental data, thanks to the highly efficient and stable  $\text{CO}_2\text{RR}$  to CO on the  $\text{Sb}_{0.22}\text{Cu}$  electrode. Tafel analysis is considered one of the most important tools in the mechanism prediction, even though it has some limitations [69]. As shown in Figure 7d, the Tafel plot is built by plotting overpotential as function of CO partial current density ( $j_{\text{CO}}$ ) in logarithm scale. A Tafel slope of  $69 \text{ mV dec}^{-1}$  is obtained at low overpotentials ( $\eta < 300 \text{ mV}$ ), which is close to  $56 \text{ mV dec}^{-1}$ , indicating a chemical step (e.g. proton transfer) as the rate-limiting step, following a first electron transfer or a first coupled electron-proton transfer. This outcome is in agreement with a recent work by Nørskov *et al.* [70], in which it is found that the electron transfer to adsorbed  $^*\text{CO}_2$  is very facile and thus unlikely to be rate-determining in  $\text{CO}_2$  adsorption.

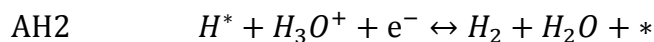
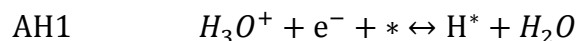
Assuming, then, an electron-proton transfer as the first step,  $\text{CO}_2\text{RR}$  can proceed through the following steps, where hydronium ions in the solution are the proton sources



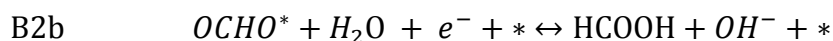
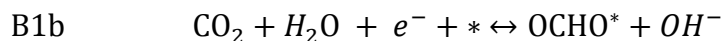
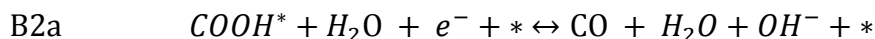
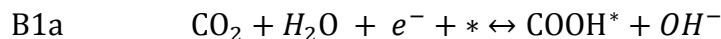
leading to CO production, or through



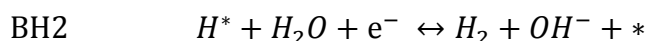
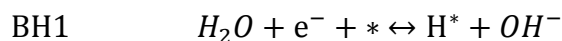
yielding formic acid. In competition to CO<sub>2</sub>RR, HER will unfold through the Volmer and Heyrovsky steps as



We do not consider the Tafel path for HER since on the catalyst surface H<sub>2</sub> dissociation is strongly disfavored due to the alternating presence of Cu and Sb atoms (H does not bind at Sb sites). CO<sub>2</sub>RR can also proceed with water as proton source, through the following steps



Similarly, HER will unfold via the alkaline Volmer-Heyrovsky mechanism



The free energy diagrams with activation barriers of CO<sub>2</sub>RR unfolding along the steps A (A1a+A2a toward CO and A1b+A2b toward HCOOH) and of HER along steps AH (AH1+AH2), at pH=6.8 and U=-0.5 V, are reported in Figure 8a. The intermediate state geometries of \*COOH, \*OCHO and \*H are reported in Figure 8c-d. Transition state geometries are reported in Figure S17 for completeness. From Figure 8a, it is possible to notice that step AH1 shows the lowest activation barrier and HER proceeds through proton consumption. When the applied potential is lowered and the reaction rate

increases significantly, HER through AH1 and AH2 steps will be limited by proton diffusion from the bulk, determining an increase of local pH in the double layer [46, 47, 71, 72]. The proton depletion in the double layer implies that reactions can proceed only from water splitting, unfolding along the B pathways. In Figure 8b we report the free energy diagram with activation barriers of CO<sub>2</sub>RR following steps B (B1a+B2a toward CO and B1b+B2b toward HCOOH) and of HER along steps BH (BH1+BH2) at U=-1.0 V and pH=9. It is worth to note that the barrier of step BH1 is higher than the activation energy of step B1a, implying that HER is now disfavored with respect to CO<sub>2</sub>RR via the \*COOH intermediate. We also notice that the barriers of steps A1b and B1b are always higher than those of A1a and B1a, respectively, disfavoring HCOOH production. The interplay between the kinetics of surface reactions, local pH and mass transport is therefore crucial to understand the mechanism of CO<sub>2</sub>RR. At high potentials, HER is favored or competing with CO<sub>2</sub>RR, since diffusion can keep up with proton consumption at the surface. At more negative potentials, acidic HER is hindered by proton depletion in the double layer, which, in turn, causes an increase of local pH and a switch to the alkaline mechanisms. In the latter case, our calculations unveil that the Cu-Sb stepped surface presents a kinetic barrier for step B1a on our catalyst lower than that for BH1, thus favoring the \*COOH intermediate. The surface morphology is also crucial in the following steps, since (see Figure 8a,b), on this surface, adsorbed \*CO, resulted from \*COOH protonation, readily desorbs to CO(g), implying that electroreduction does not proceed further and the main product is indeed CO. Concisely, Sb plays a critically important role in the CO<sub>2</sub>RR to CO process on the bimetallic catalyst by stabilizing stepped Cu surfaces selective for the reaction, lowering energy barriers for the formation of key intermediate and favouring the CO desorption instead of its further reduction. This explains the excellent performance of the optimal Sb-Cu catalyst for the desired reaction pathway.

## 4. Conclusions

We have presented a Sb-Cu catalyst for effective CO<sub>2</sub>RR to CO. The bimetallic material is successfully synthesized through a simple, green and upscalable route. Detailed analyses suggest that addition of Sb has promoted the formation of nanocrystalline Cu<sub>2</sub>O particles with a narrow size distribution. The Sb element is homogeneously incorporated into the Cu<sub>2</sub>O structure without formation of other crystalline phases at high contents, in accordance with the theoretical study that the formation of Sb clusters on the surface is thermodynamically unfavored. The optimized Sb-Cu bimetallic catalyst achieves excellent selectivity and high activity for the CO formation, and demonstrates good durability in a wide current density range. Detailed ab initio simulations firstly elucidate the origin of high performance of the Sb-Cu catalyst in the CO<sub>2</sub>RR to CO process, giving new insights into the development of multimetallic catalysts for the CO<sub>2</sub> conversion to a desired product. As the most important C<sub>1</sub>-building block, CO has high relevance for the chemical industry



and is intensively used in large industrial processes such as Fischer-Tropsch synthesis of hydrocarbons and Monsanto/Cativa acetic acid synthesis. The herein proposed Sb-Cu material is low-cost and the fabrication method is environmentally friendly and energetically convenient, allowing their mass-scale production. Hence, it possesses good potential to be implemented in advanced CO<sub>2</sub> electrolysis technologies such as gas diffusion electrodes and zero-gap electrolyzers to enable industrial scale CO<sub>2</sub> conversion to CO. The present work highlights the versatility of Cu-based electrocatalysts and the importance of rational design of Cu multimetallic materials for the CO<sub>2</sub>RR application.

## Acknowledgements

Dr. Zeng contributed to the conceptualization, the synthesis and electrochemical analyses. Dr. Re Fiorentina, Dr. Risplendi and Prof. Cicero contributed to the ab initio simulations. Dr. Castellino contributed to XPS investigation and the corresponding data analysis. Dr. Fontana contributed to FESEM and TEM investigations as well as XRD fitting. Dr. Sacco contributed to the EIS fitting and mass diffusion modelling. Dr. Farkhondehfal contributed to the HPLC analysis. Dr. Drago contributed to the ICP-OES analysis. Prof. Pirri contributed to the resources. All authors contributed to the composition of the manuscript.

## Conflict of Interest

The authors declare no competing interests.

## References

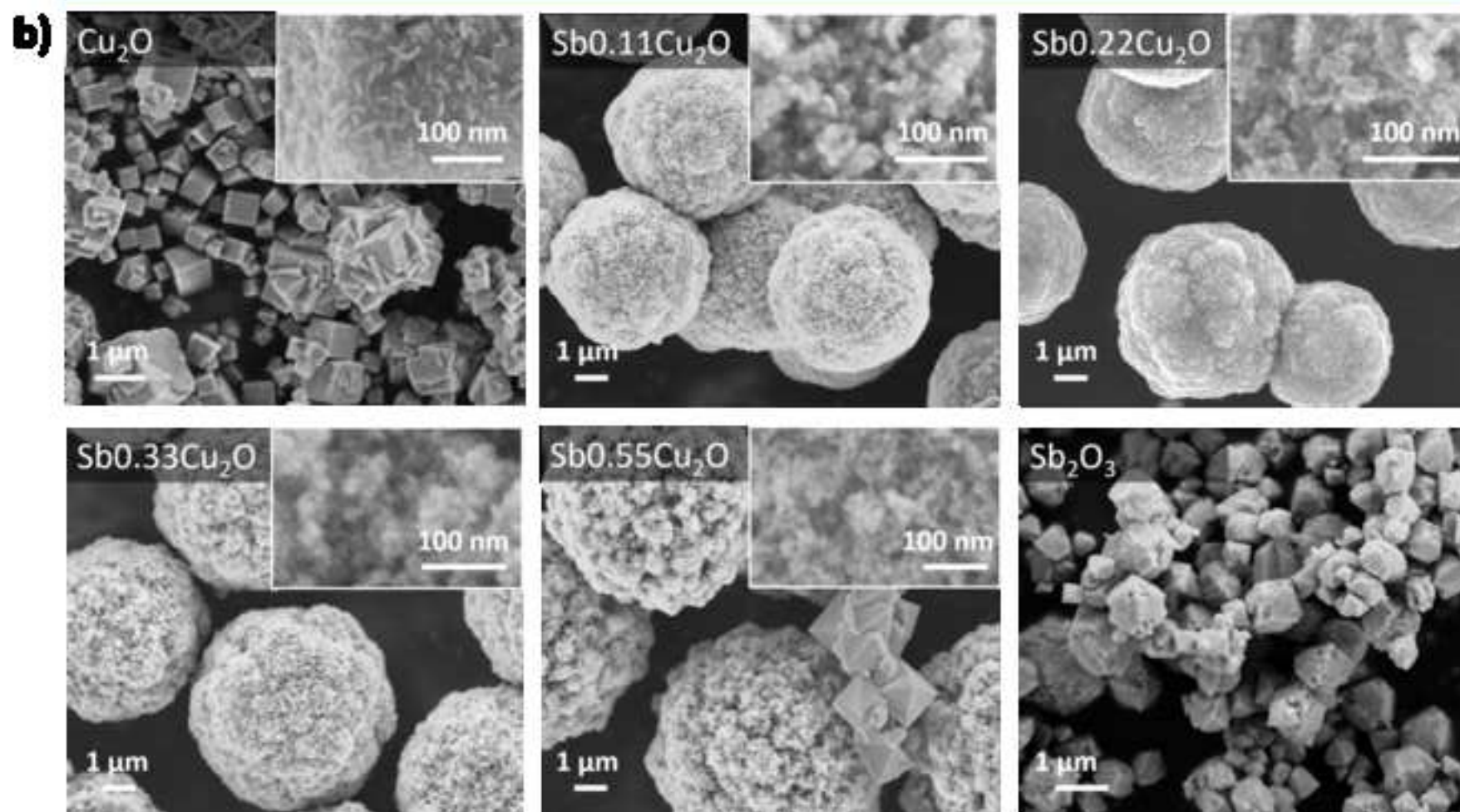
- [1] A. Sacco, R. Speranza, U. Savino, J. Zeng, M. A. Farkhondehfal, A. Lamberti, A. Chiodoni, C. F. Pirri, *ACS Sustainable Chem. Eng.* 8 (2020) 7563-7568.
- [2] T. N. Huan, D. A. D. Corte, S. Lamaison, D. Karapinar, L. Lutz, N. Menguy, M. Foldyna, S. -H. Turren-Cruz, A. Hagfeldt, F. Bella, M. Fontecave, V. Mougél, *PNAS* 116 (2019) 9735-9740.
- [3] Gurudayal, J. Bullock, D. F. Srankó, C. M. Towle, Y. Lum, M. Hettick, M. C. Scott, A. Javey, J. Ager, *Energy Environ. Sci.* 10 (2017) 2222-2230.
- [4] M. Schreier, F. Héroguel, L. Steier, S. Ahmad, J. S. Luterbacher, M. T. Mayer, J. Luo, M. Grätzel, *Nat. Energy* 2 (2017) 17087.
- [5] M. Schreier, L. Curvat, F. Giordano, L. Steier, A. Abate, S. M. Zakeeruddin, J. Luo, M. T. Mayer, M. Grätzel, *Nat. Commun.* 6 (2015) 7326.
- [6] Y. Hori, K. Kikuchi, S. Suzuki, *Chem. Lett.* 14 (1985) 1695-1698.
- [7] Y. Hori, H. Wakebe, T. Tsukamoto, O. Koga, *Electrochim. Acta* 39 (1994) 1833-1839.

- [8] A. A. Peterson, F. Abild-Pedersen, F. Studt, J. Rossmeisl, J. K. Nørskov, *Energy Environ. Sci.* 3 (2010) 1311-1315.
- [9] A. A. Peterson, J. K. Nørskov, *J. Phys. Chem. Lett.* 3 (2012) 251-258.
- [10] A. Bagger, W. Ju, A. S. Varela, P. Strasser, J. Rossmeisl, *ChemPhysChem* 18 (2017) 3266-3273.
- [11] S. Nitopi, E. Bertheussen, S. B. Scott, X. Liu, A. K. Engstfeld, S. Horch, B. Seger, I. E. L. Stephens, K. Chan, C. Hahn, J. K. Nørskov, T. F. Jaramillo, I. Chorkendorff, *Chem. Rev.* 119 (2019) 7610-7672.
- [12] J. Zhao, S. Xue, J. Barber, Y. Zhou, J. Meng, X. Ke, *J. Mater. Chem. A* 8 (2020) 4700-4734.
- [13] S. Chu, X. Li, A. W. Robertson, Z. Sun, *Acta Phys. -Chim. Sin.* 37 (2021) 2009023.
- [14] P. De Luna, R. Quintero-Bermudez, C. -T. Dinh, M.B. Ross, O. S. Bushuyev, P. Todorović, T. Regier, S. O. Kelley, P. Yang, E. H. Sargent, *Nat. Catal.* 1 (2018) 103-110.
- [15] L. Hao, Z. Sun, *Acta Phys. -Chim. Sin.* 37 (2021) 2009033.
- [16] C. W. Lee, K. D. Yang, D. -H. Nam, J. H. Jang, N. H. Cho, S. W. Im, K. T. Nam, *Adv. Mater.* 30 (2018) 1704717.
- [17] C. G. Morales-Guio, E. R. Cave, S. A. Nitopi, J. T. Feaster, L. Wang, K. P. Kuhl, A. Jackson, N. C. Johnson, D. N. Abram, T. Hatsukade, C. Hahn, T. F. Jaramillo, *Nat. Catal.* 1 (2018) 764-771.
- [18] S. Ajmal, Y. Yang, K. Li, M. A. Tahir, Y. Liu, T. Wang, A. -U. -R. Bacha, Y. Feng, Y. Deng, L. Zhang, *J. Phys. Chem. C* 123 (2019) 11555-11563.
- [19] T. T. H. Hoang, S. Verma, S. Ma, T. T. Fister, J. Timoshenko, A. I. Frenkel, P. J. A. Kenis, A. A. Gewirth, *J. Am. Chem. Soc.* 140 (2018) 5791-5797.
- [20] X. Zheng, Y. Ji, J. Tang, J. Wang, B. Liu, H. -G. Steinrück, K. Lim, Y. Li, M. F. Toney, K. Chan, Y. Cui, *Nat. Catal.* 2 (2019) 55-61.
- [21] W. Ju, J. Zeng, K. Bejtka, H. Ma, D. Rentsch, M. Castellino, A. Sacco, C. F. Pirri, C. Battaglia, *ACS Appl. Energy Mater.* 2 (2019) 867-872.
- [22] J. Zeng, K. Bejtka, W. Ju, M. Castellino, A. Chiodoni, A. Sacco, M. A. Farkhondehfar, S. Hernández, D. Rentsch, C. Battaglia, C. F. Pirri, *Appl. Catal. B* 236 (2018) 475-482.
- [23] G. O. Barasa, T. Yu, X. Lu, X. Zhou, H. Wang, L. Qian, Y. Yu, L. Liu, P. Lei, *Electrochim. Acta* 295 (2019) 584-590.
- [24] Z. B. Hoffman, T. S. Gray, Y. Xu, Q. Lin, T. B. Gunnoe, G. Zangari, *ChemSusChem* 12 (2019) 231-239.
- [25] X. Zhang, X. Sun, S. -X. Guo, A. M. Bond, J. Zhang, *Energy Environ. Sci.* 12 (2019) 1334-1340.
- [26] J. Medina-Ramos, R. C. Pupillo, T. P. Keane, J. L. DiMeglio, J. Rosenthal, *J. Am. Chem. Soc.* 137 (2015) 5021-5027.

- [27] F. Li, M. Xue, J. Li, X. Ma, L. Chen, X. Zhang, D. R. MacFarlane, J. Zhang, *Angew. Chem. Int. Ed.* 56 (2017) 14718-14722.
- [28] M. Jia, S. Hong, T. -S. Wu, X. Li, Y. -L. Soo, Z. Sun, *Chem. Commun.* 55 (2019) 12024-12027.
- [29] Y. Li, S. Chu, H. Shen, Q. Xia, A. W. Robertson, J. Masa, U. Siddiqui, Z. Sun, *ACS Sustainable Chem. Eng.* 8 (2020) 4948-4954.
- [30] S. Mou , Y. Li, L. Yue, J. Liang, Y. Luo, Q. Liu, T. Li, S. Lu, A. M. Asiri, X. Xiong, D. Ma, X. Sun, *Nano Res.* 14 (2021) 2831-2836.
- [31] Z. Zhang, Y. Yang, W. Li, W. Zhang, M. Liu, Z. Weng, S. Huo, J. Zhang, *J. Colloid Interface Sci.* 601 (2021) 661-668.
- [32] H. Li, T.-W. Jiang, X. Qin, J. Chen, X.-Y. Ma, K. Jiang, X.-G. Zhang, W.-B. Cai, *ACS Catal.* 2021, 11, 6846-6856.
- [33] S. Jia, Q. Zhu, H. Wu, M. Chu, S. Han, R. Feng, J. Tu, J. Zhai, B. Han, *Chinese J. Catal.* 41 (2020) 1091-1098.
- [34] L. Lutterotti, S. Matthies, H. -R. Wenk, *J. Appl. Phys.* 81 (1997) 594-600.
- [35] A. Sacco, J. Zeng, K. Bejtka, A. Chiodoni, *J. Catal.* 372 (2019) 39-48.
- [36] N. Gupta, M. Gattrell, B. MacDougall, *J. Appl. Electrochem.* 36 (2006) 161-172.
- [37] L. Mandal, K. R. Yang, M. R. Motapothula, D. Ren, P. Lobaccaro, A. Patra, M. Sherburne, V. S. Batista, B. S. Yeo, J. W. Ager, J. Martin, T. Venkatesan, *ACS Appl. Mater. Interfaces* 10 (2018) 8574-8584.
- [38] A. van de Walle, M. Asta, G. Ceder, *Calphad* 26 (2002) 539-553.
- [39] P. Giannozzi, S. Baroni, N. Bonini, M. Calandra, R. Car, C. Cavazzoni, D. Ceresoli, G. L. Chiarotti, M. Cococcioni, I. Dabo, A. Dal Corso, S. Fabris, G. Fratesi, S. de Gironcoli, R. Gebauer, U. Gerstmann, C. Gougoussis, A. Kokalj, M. Lazzeri, L. Martin-Samos, N. Marzari, F. Mauri, R. Mazzarello, S. Paolini, A. Pasquarello, L. Paulatto, C. Sbraccia, S. Scandolo, G. Sclauzero, A. P. Seitsonen, A. Smogunov, P. Umari, R. M. Wentzcovitch, *J. Phys.: Condens. Matter* 21 (2009) 395502.
- [40] P. Giannozzi, O. Andreussi, T. Brumme, O. Bunau, M. Buongiorno Nardelli, M. Calandra, R. Car, C. Cavazzoni, D. Ceresoli, M. Cococcioni, N. Colonna, I. Carnimeo, A. Dal Corso, S. de Gironcoli, P. Delugas, R. A. DiStasio Jr, A. Ferretti, A. Floris, G. Fratesi, G. Fugallo, R. Gebauer, U. Gerstmann, F. Giustino, T. Gorni, J. Jia, M. Kawamura, H.-Y. Ko, A. Kokalj, E. Küçükbenli, M. Lazzeri, M. Marsili, N. Marzari, F. Mauri, N. L. Nguyen, H.-V. Nguyen, A. Otero-de-la-Roza, L. Paulatto, S. Poncé, D. Rocca, R. Sabatini, B. Santra, M. Schlipf, A. P. Seitsonen, A. Smogunov, I. Timrov, T. Thonhauser, P. Umari, N. Vast, X. Wu, S. Baroni, *J. Phys.: Condens. Matter* 29 (2017) 465901.
- [41] A. van de Walle, G. Ceder, *JPE* 23 (2002) 348.

- [42] F. Raffone, C. Ataca, J. C. Grossman, G. Cicero, *J. Phys. Chem. Lett.* 7 (2016) 2304-2309.
- [43] A. K. Verma, F. Raffone, G. Cicero, *Nanomater. Nanotechnol.* 10 (2020) 1-6.
- [44] J. K. Nørskov, J. Rossmeisl, A. Logadottir, L. Lindqvist, J. R. Kitchin, T. Bligaard, H. Jónsson, *J. Phys. Chem. B* 108 (2004) 17886-17892.
- [45] X. Nie, M. R. Esopi, M. J. Janik, A. Asthagiri, *Angew. Chem. Int. Ed.* 52 (2013) 2459-2462.
- [46] X. Liu, J. Xiao, H. Peng, X. Hong, K. Chan, J. K. Nørskov, *Nat. Commun.* 8 (2017) 15438.
- [47] B. Zijlstra, X. Zhang, J.-X. Liu, I. A. W. Filot, Z. Zhou, S. Sun, E. J. M. Hensen, *Electrochim. Acta* 335 (2020) 135665.
- [48] X. Liu, P. Schlexer, J. Xiao, Y. Ji, L. Wang, R. B. Sandberg, M. Tang, K. S. Brown, H. Peng, S. Ringe, C. Hahn, T. F. Jaramillo, J. K. Nørskov, K. Chan, *Nat. Commun.* 10 (2019) 32.
- [49] M. Nolan, S. D. Elliott, *Chem. Mater.* 20 (2008) 5522-5531.
- [50] Y. Jing, Y. Liu, J. Zhao, Z. Xia, *J. Phys. Chem. Lett.* 10 (2019) 7439-7444.
- [51] T. Abendroth, B. Schumm, S. A. Alajlan, A. M. Almogbel, G. Mäder, P. Härtel, H. Althues, S. Kaskel, *Thin Solid Films* 624 (2017) 152-159.
- [52] C. D. Wagner, A. V. Naumkin, A. Kraut-Vass, J. W. Allison, C. J. Powell, J. R. Jr. Rumble, NIST Standard Reference Database 20, Version 3.4 (web version) (<http://srdata.nist.gov/xps/>) (2003).
- [53] M. Biesinger, *Surf. Interface Anal.* 49 (2017) 1325-1334.
- [54] J. B. Jonathan, E. H. Christopher, A. C. Christopher, R. B. Andrew, *Nano Lett.* 9 (2009) 2239-2242.
- [55] J. Zeng, T. Rino, K. Bejtka, M. Castellino, A. Sacco, M. A. Farkhondehfal, A. Chiodoni, F. Drago, C. F. Pirri, *ChemSusChem* 13 (2020) 4128-4139.
- [56] A. Dutta, M. Rahaman, N. C. Luedi, M. Mohos, P. Broekmann, *ACS Catal.* 6 (2016) 3804-3814.
- [57] C.-T. Dinh, F. P. G. De Arquer, D. Sinton, E. H. Sargent, *ACS Energy Lett.* 3 (2018) 2835-2840.
- [58] W. Luo, J. Zhang, M. Li, A. Züttel, *ACS Catal.* 9 (2019) 3783-3791.
- [59] M. Ma, K. Liu, J. Shen, R. Kas, W. A. Smith, *ACS Energy Lett.* 3 (2018) 1301-1306.
- [60] Y. Chen, C. W. Li, M. W. Kanan, *J. Am. Chem. Soc.* 134 (2012) 19969-19972.
- [61] J. Rosen, G. S. Hutchings, Q. Lu, S. Rivera, Y. Zhou, D. G. Vlachos, F. Jiao, *ACS Catal.* 5 (2015) 4293-4299.
- [62] Q. Lu, J. Rosen, Y. Zhou, G. S. Hutchings, Y. C. Kimmel, J. G. Chen, F. Jiao, *Nature Comm.* 5 (2014) 3242.
- [63] M. Dunwell, Q. Lu, J. M. Heyes, J. Rosen, J. G. Chen, Y. Yan, F. Jiao, B. Xu, *J. Am. Chem. Soc.* 139 (2017) 3774-3783.
- [64] A. J. Garza, A. T. Bell, M. Head-Gordon, *J. Phys. Chem. Lett.* 9 (2018) 601-606.

- [65] S. B. Scott, T. V. Hogg, A. T. Landers, T. Maagaard, E. Bertheussen, J. C. Lin, R. C. Davis, J. W. Beeman, D. Higgins, W. S. Drisdell, C. Hahn, A. Mehta, B. Seger, T. F. Jaramillo, I. Chorkendorff, *ACS Energy Lett.* 4 (2019) 803-804.
- [66] Y. Lum, J. W. Ager, *Angew. Chem. Int. Ed.* 57 (2018) 551-554.
- [67] Q. Lei, H. Zhu, K. Song, N. Wei, L. Liu, D. Zhang, J. Yin, X. Dong, K. Yao, N. Wang, X. Li, B. Davaasuren, J. Wang, Y. Han, *J. Am. Chem. Soc.* 142 (2020) 4213-4222.
- [68] S. Jiang, K. Klingan, C. Pasquini, H. Dau, *J. Chem. Phys.* 150 (2019) 041718.
- [69] M. Dunwell, W. Luc, Y. Yan, F. Jiao, B. Xu, *ACS Catal.* 8 (2018) 8121-8129.
- [70] J. A. Gauthier, M. Fields, M. Bajdich, L. D. Chen, R. B. Sandberg, K. Chan, J. K. Nørskov, *J. Phys. Chem. C* 123 (2019) 29278-29283.
- [71] P. S. Lamoureux, A. R. Singh, K. Chan, *ACS Catalysis* 9 (2019) 6194-6201.
- [72] V. Grozovski, S. Vesztergom, G. Láng, P. Broekmann, *J. Electrochem. Soc.* 164 (2017) E3171-E3178.



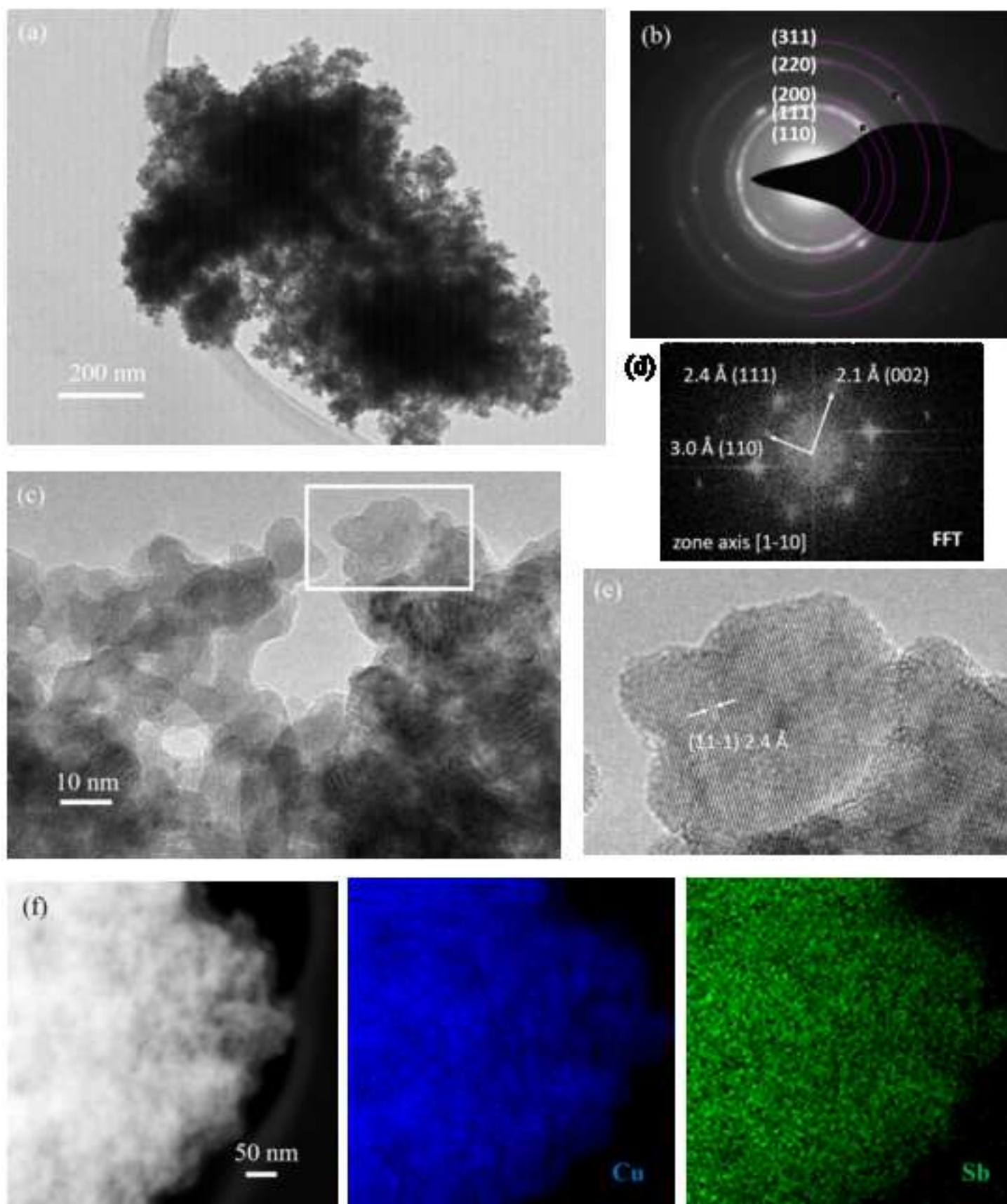
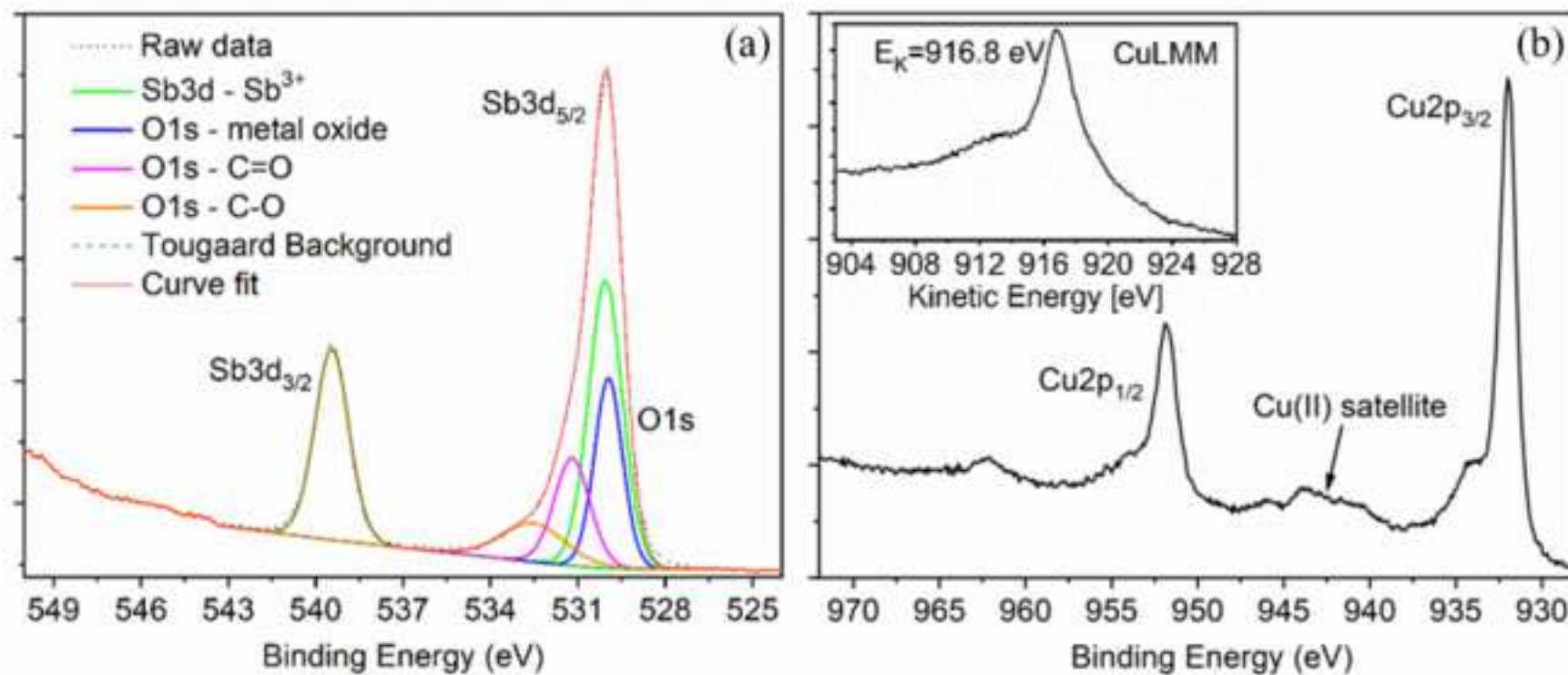
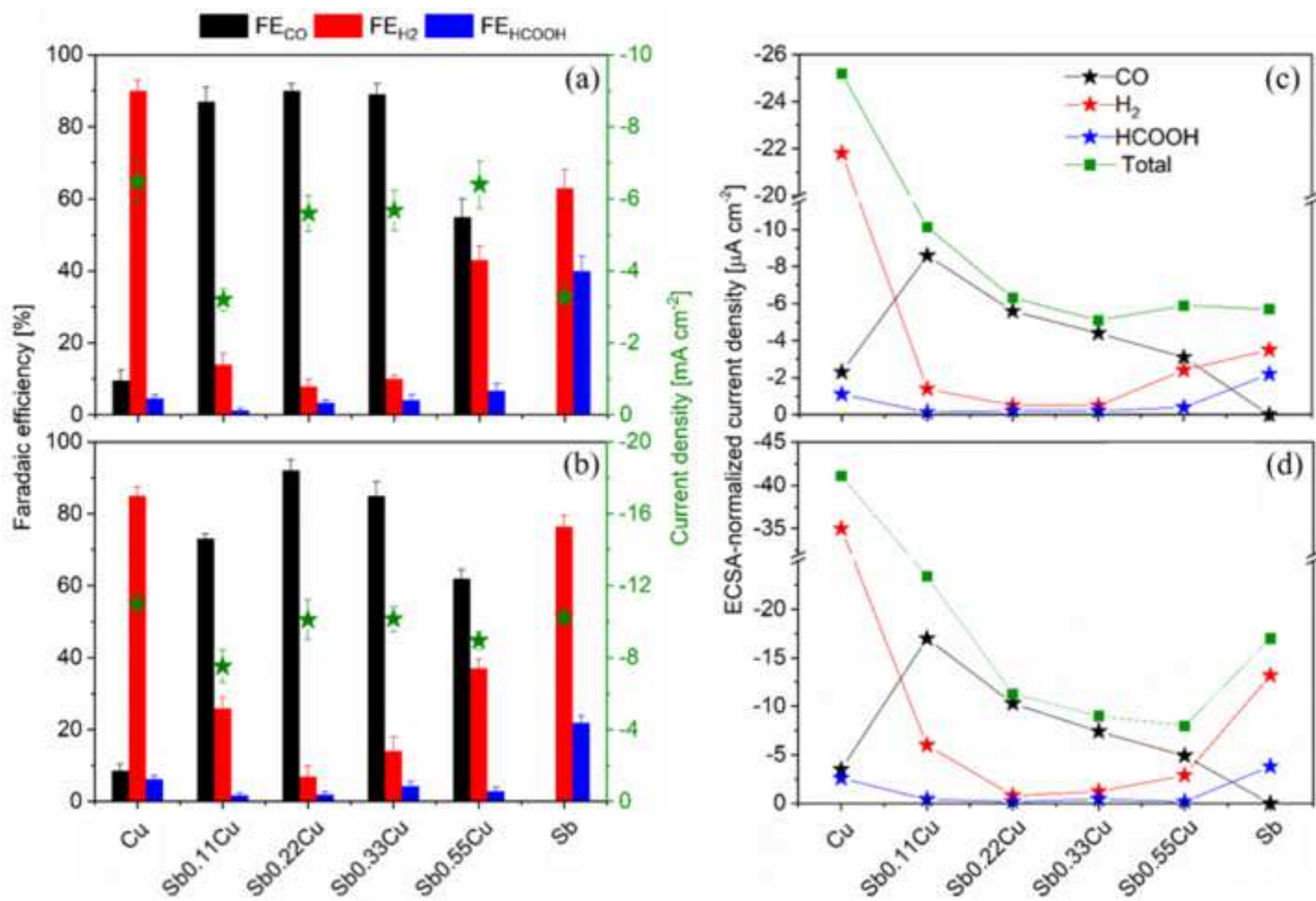


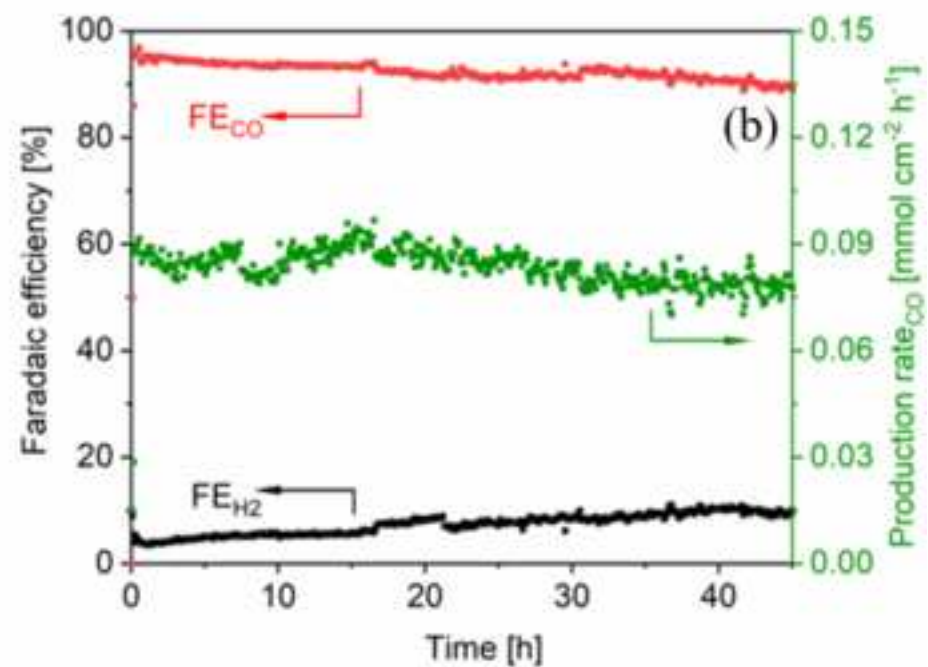
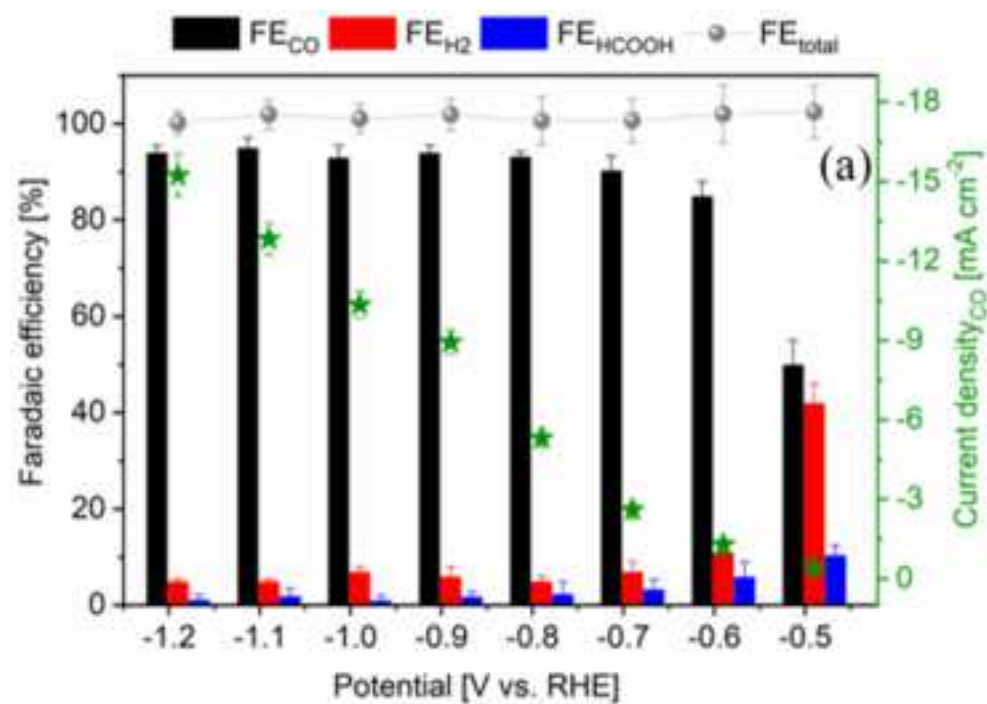


Figure 3









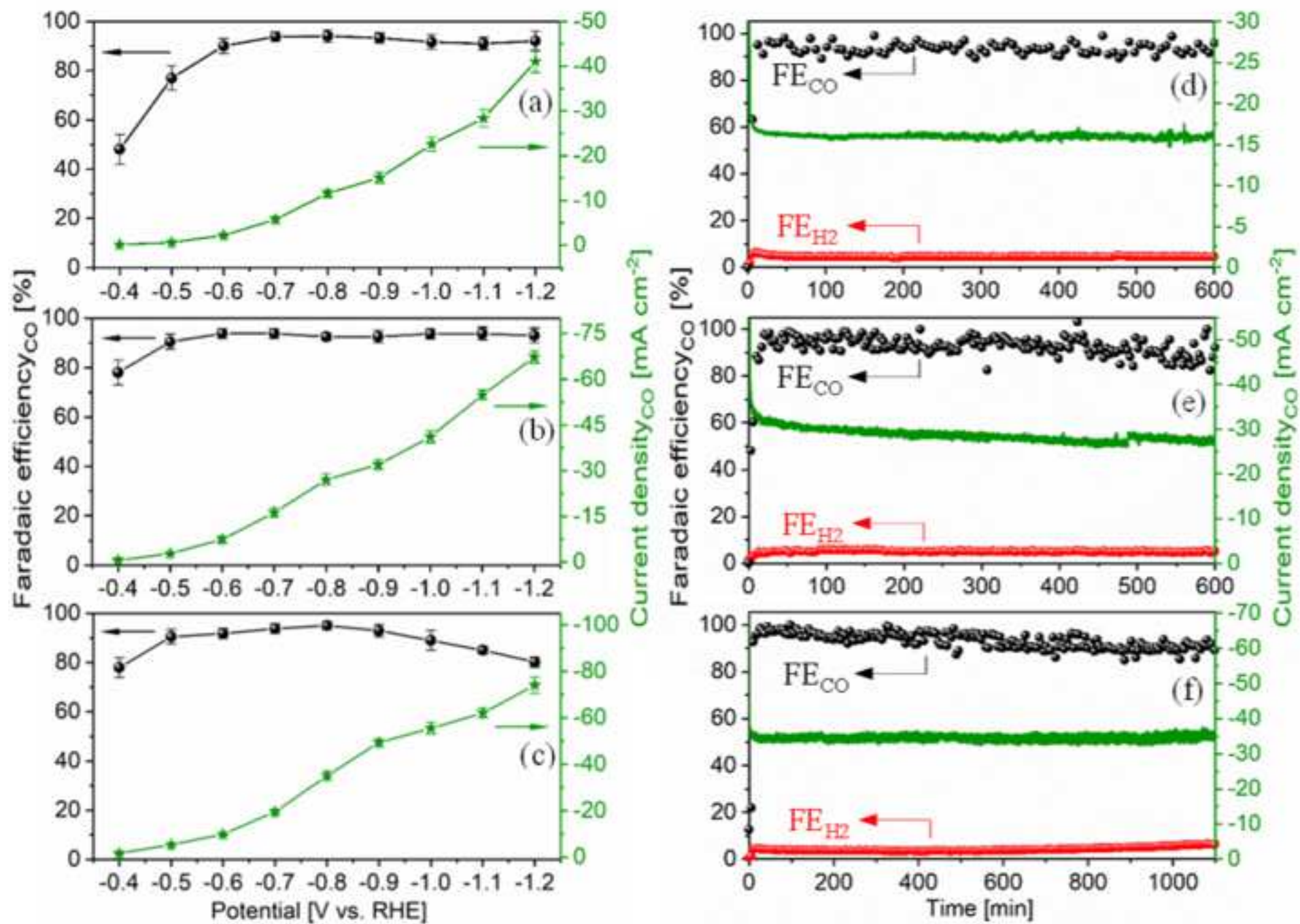


Figure 7

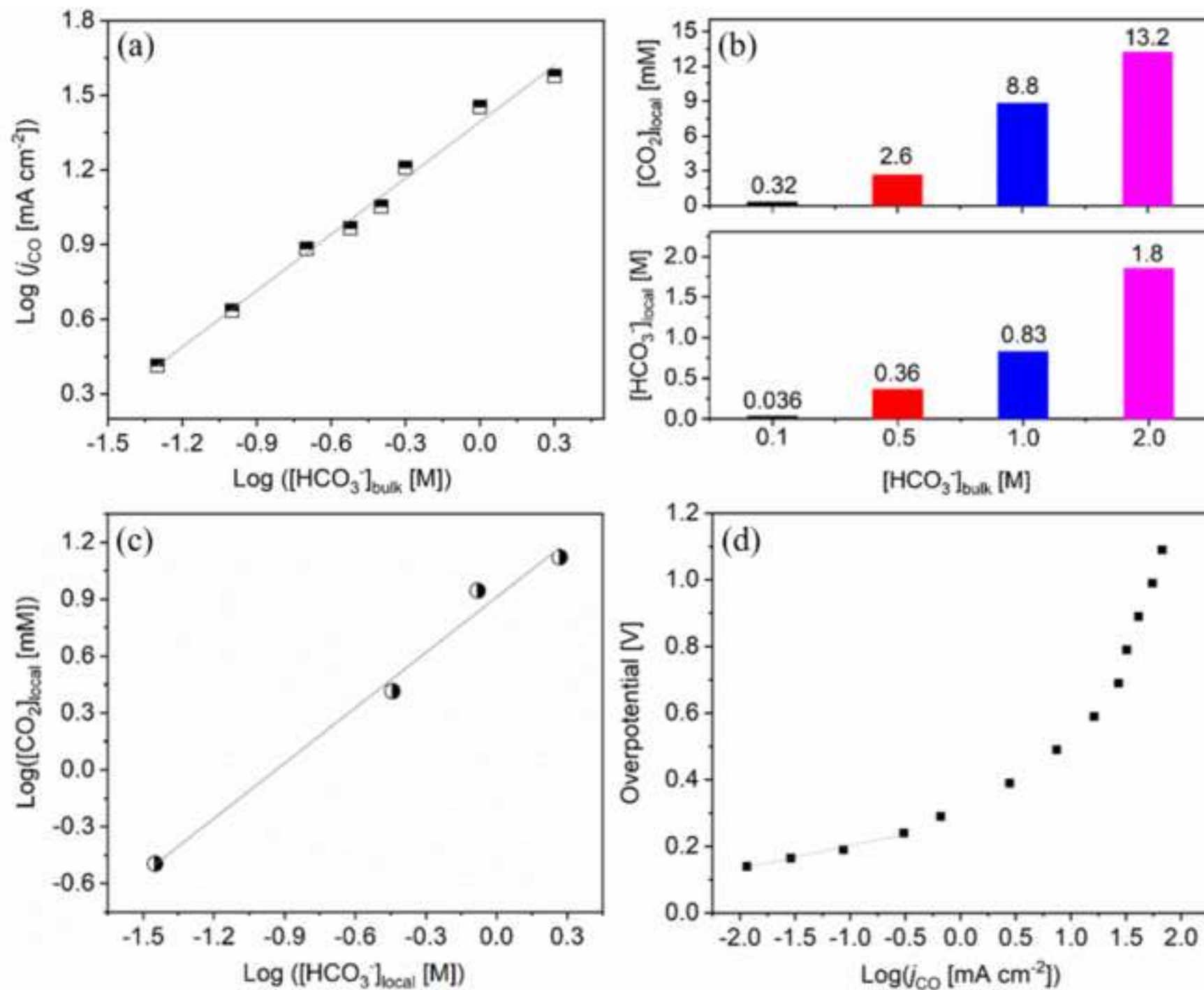
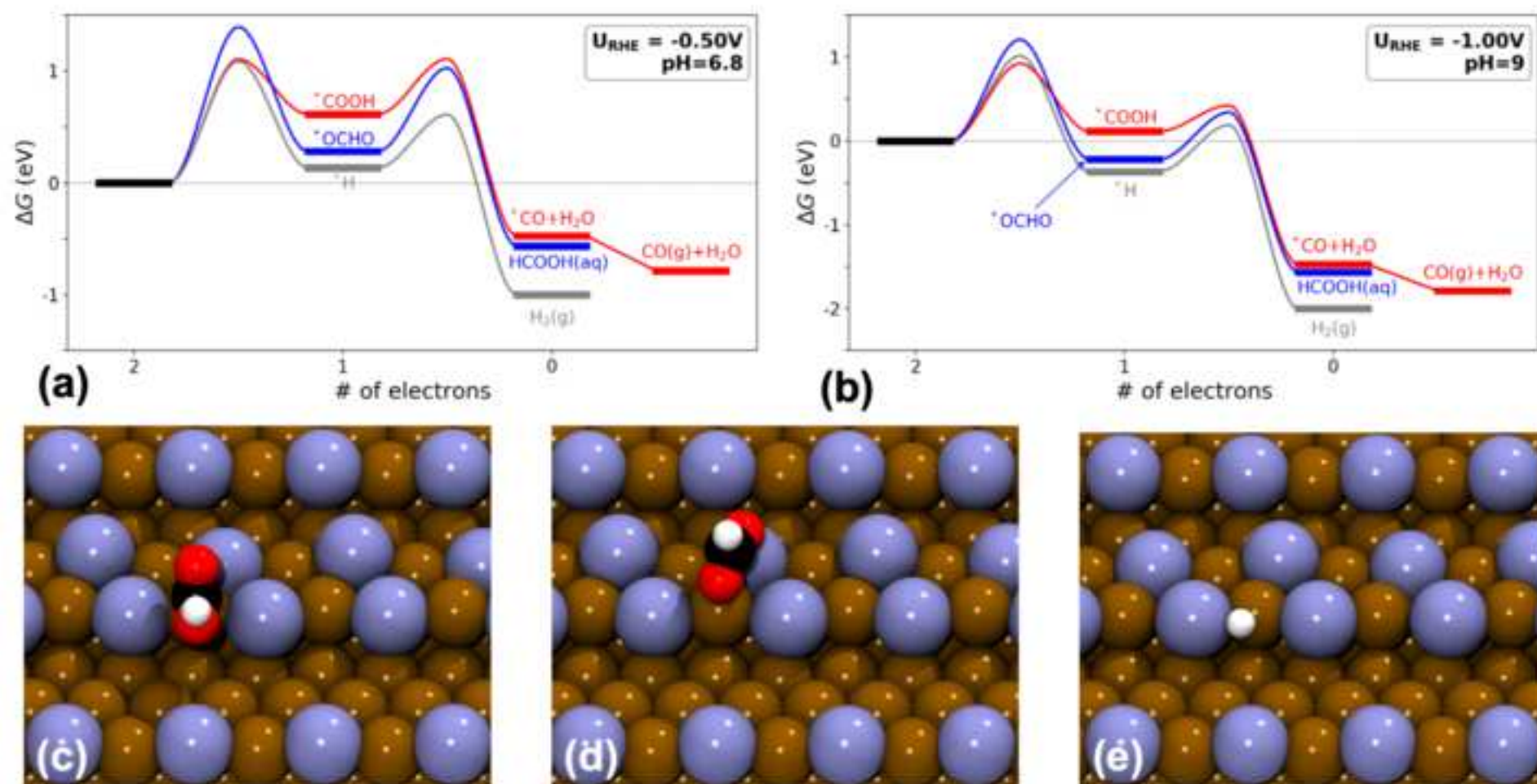
[Click here to access/download;Figure;FIG7.png](#)



Figure 8

[Click here to access/download;Figure;Fig8.tiff](#)



## Figure Captions

Figure 1 (a) Schematic of a typical synthesis process. FESEM images of the materials: (b)  $\text{Cu}_2\text{O}$ , (c)  $\text{Sb}_{0.11}\text{Cu}_2\text{O}$ , (d)  $\text{Sb}_{0.22}\text{Cu}_2\text{O}$ , (e)  $\text{Sb}_{0.33}\text{Cu}_2\text{O}$ , (f)  $\text{Sb}_{0.55}\text{Cu}_2\text{O}$  and (g)  $\text{Sb}_2\text{O}_3$ .

Figure 2 TEM characterization of the  $\text{Sb}_{0.22}\text{Cu}_2\text{O}$  sample: (a) low-magnification image with related (b) SAED pattern, (c) HR investigation of the highlighted region with the FFT (d) of the corresponding HRTEM image (e). (f) HAADF STEM image alongside EDX elemental maps for Cu and Sb elements.

Figure 3 XPS spectra of  $\text{Sb}_{0.22}\text{Cu}_2\text{O}$  sample: (a) HR XPS analysis of Sb element and (b)  $\text{Cu}2p$  doublet region acquired in HR mode and Auger  $\text{CuLMM}$  region in inset.

Figure 4 FE values and geometric current densities at various electrodes in 0.1 M  $\text{KHCO}_3$  electrolyte under applied potential: (a) -0.8 V and (b) -1.0 V. ECSA-normalized partial and total current densities at various electrodes under applied potential: (c) -0.8 V and (d) -1.0 V.

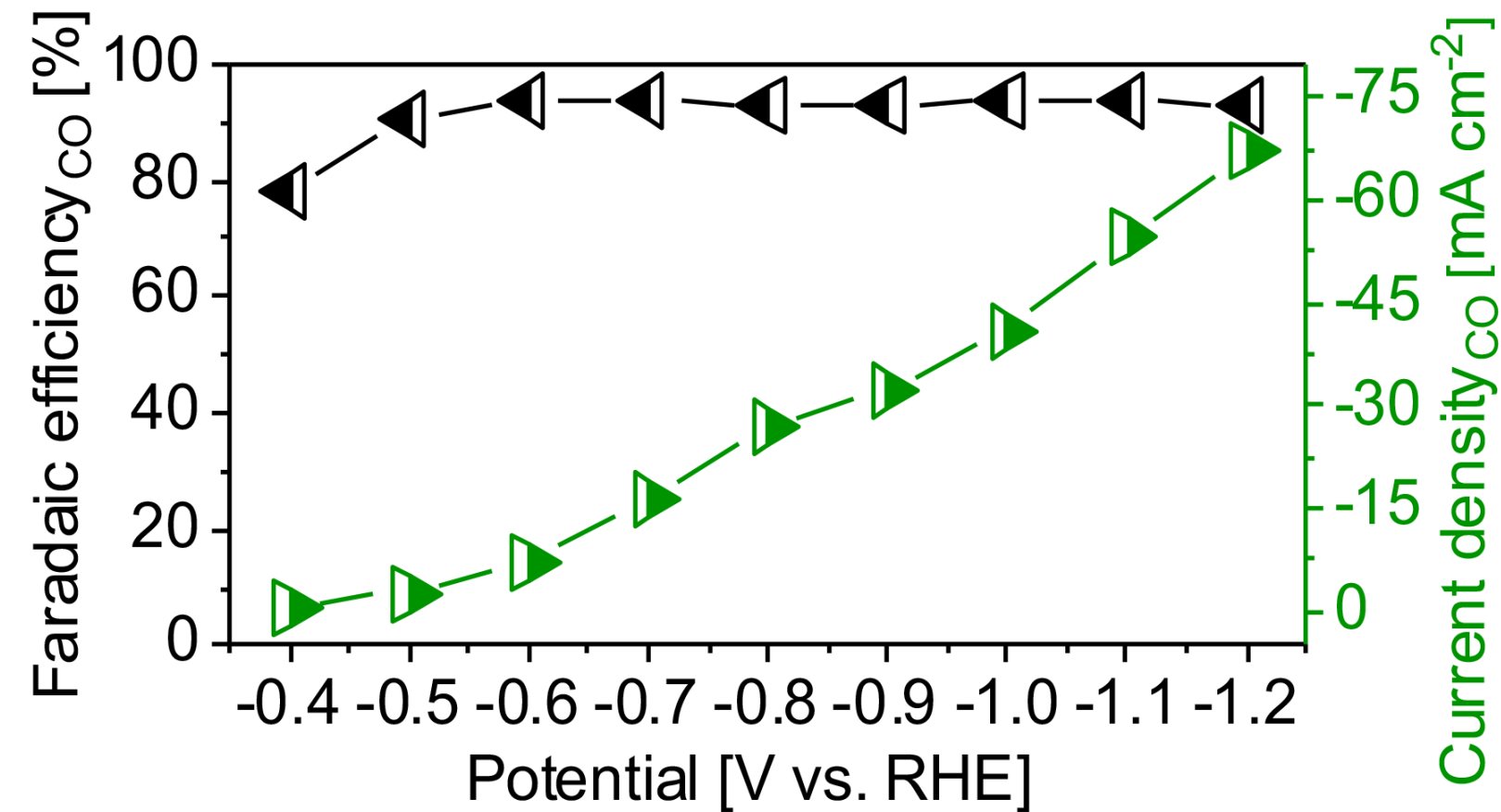
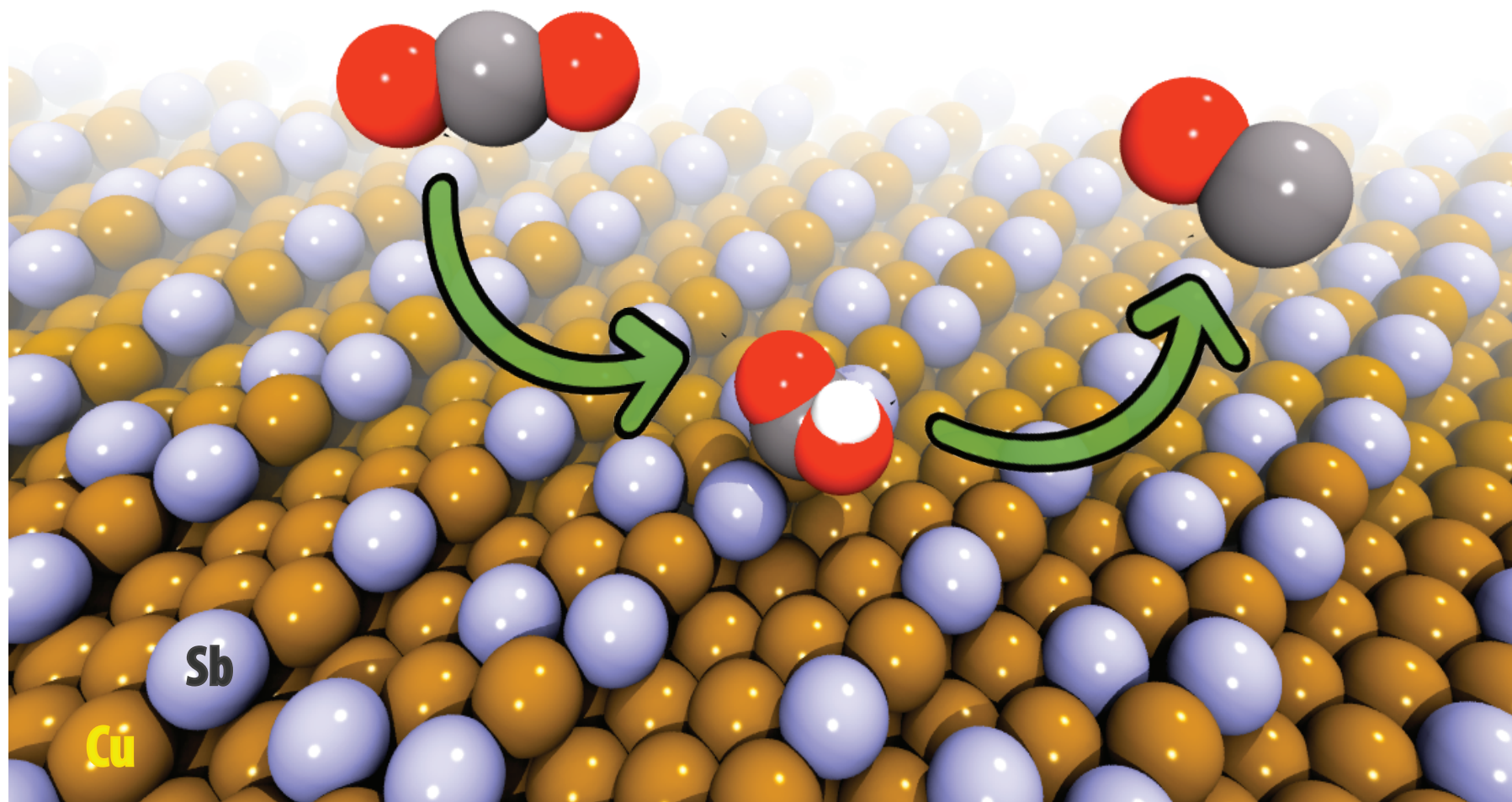
Figure 5  $\text{CO}_2\text{RR}$  on the  $\text{Sb}_{0.22}\text{Cu}$  electrode in 0.1 M  $\text{KHCO}_3$  electrolyte: (a) FE values for various products and current densities for CO formation at various applied potentials and (b) FE values for main products and production rate of CO during a long-term stability test at -0.8 V.

Figure 6  $\text{CO}_2\text{RR}$  on the  $\text{Sb}_{0.22}\text{Cu}$  electrode: FE values and current densities for CO formation at various applied potential in  $\text{KHCO}_3$  electrolyte with different concentrations (a) 0.5 M, (b) 1.0 M and (c) 2.0 M; FE values for main gas products and current densities for CO formation at -0.8 V in  $\text{KHCO}_3$  electrolyte with various concentrations (d) 0.5 M, (e) 1.0 M and (f) 2.0 M.

Figure 7 Dependence of CO formation rate on the bulk  $\text{HCO}_3^-$  concentration at -0.8 V (a),  $[\text{CO}_2]_{\text{local}}$  and  $[\text{HCO}_3^-]_{\text{local}}$  as function of  $[\text{HCO}_3^-]_{\text{bulk}}$  at -1.2 V (b), dependence of  $[\text{CO}_2]_{\text{local}}$  on  $[\text{HCO}_3^-]_{\text{local}}$  at -1.2 V (c) and Tafel plot at  $\text{Sb}_{0.22}\text{Cu}$  electrode in 1.0 M  $\text{KHO}_3$  electrolyte (d).

Figure 8 Reaction energy diagrams for the dissociation of  $\text{CO}_2$  at -0.5 V vs RHE at pH 6.8 (a) and at -1.0 V vs RHE at pH 9 (b) on  $\text{Sb}_x\text{Cu}_{(1-x)}(211)$  surface with  $x=0.33$ ; (red) electrochemical reduction to CO; (blue) electrochemical reduction to  $\text{HCOOH}$ ; (grey) hydrogen evolution reaction. Top view of intermediate state geometries for the adsorption of  $\text{COOH}$  (c),  $\text{OCHO}$  (d) and H (e) on  $\text{Sb}_x\text{Cu}_{(1-x)}(211)$

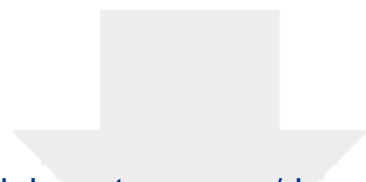
surface with  $x=0.33$ . Cu atoms are represented in ochre, Sb atoms in iceblue, C atoms in black, O atoms in red and H in white.





## Highlights

- ✚ Sb-Cu<sub>2</sub>O material is synthesized via a one-pot microwave-assisted route.
- ✚ Sb is uniformly distributed and promotes the formation of nanocrystalline Cu<sub>2</sub>O.
- ✚ The derived Sb-Cu shows outstanding performance for the CO<sub>2</sub>RR to CO.
- ✚ Enhancing local CO<sub>2</sub> concentration is demonstrated to boost CO formation rate.
- ✚ Theoretical study reveals the critical roles of Sb in CO formation on Sb-Cu.



[Click here to access/download](#)

**Supplementary Material**

Supporting information-revised-clean.docx

